

## ABSTRACT

FAUGL, TIMOTHY ALLEN. Modeling of Visualization Cyclotron Target with Coupling of Proton Range and Target Density. (Under the direction of Dr. J. M. Doster and Dr. M. Stokely.)

$^{18}\text{F}$  for medical imaging is commonly produced via the  $^{18}\text{O}(\text{p},\text{n})^{18}\text{F}$  reaction by proton irradiation of batch-style water targets. Previous computational modeling of targets of this type has been performed by implementing a volume averaged void fraction that corresponds to limiting conditions within a target. To determine the spatial distribution of void, the radiation transport model must be dependent upon fluid density and vice versa. An algorithm was developed and implemented in a computational model that coupled the radiation transport data with a fluid property distribution for single-phase conditions. The computational model was based on a proprietary visualization target from BTI Targetry, LLC. The visualization target enabled validation of the computational model.

© Copyright 2014 by Timothy Allen Faugl

All Rights Reserved

Modeling of Visualization Cyclotron Target with Coupling of Proton Range and Target  
Density

by  
Timothy Allen Faugl

A thesis submitted to the Graduate Faculty of  
North Carolina State University  
in partial fulfillment of the  
requirements for the Degree of  
Master of Science

Nuclear Engineering

Raleigh, North Carolina

2014

APPROVED BY:

---

Dr. R. White

---

Dr. I. Bolotnov

---

Dr. J. M. Doster  
Co-chair of Advisory Committee

---

Dr. M. Stokely  
Co-chair of Advisory Committee

## **BIOGRAPHY**

Timothy Allen Faugl was born on October 31, 1988 to Sherry and Timothy Faugl. He lived in Aiken, SC and graduated from South Aiken High School in May of 2006. He attended the College of Charleston and graduated in May 2010 with a Bachelors of Science in Physics. He continued his education at Greenville Technical College by studying Mechanical Engineering. Combining his interests in nuclear physics and engineering, he decided to continue his education by pursuing a graduate level degree in Nuclear Engineering at North Carolina State University.

## ACKNOWLEDGEMENTS

I would like to thank all members of my graduate committee. The advice and support from Dr. J. M. Doster was critical to the success of the project. Also, I would like to thank Dr. M. Stokely for his instruction and experience in the implementation of MCNPX, as well as other areas. I would like to extend thanks to Dr. I. Bolotnov for sharing his knowledge and expertise in CFD. Special thanks also go to Dr. B. Wieland, as well as Dr. J. Peeples and Michael Poorman, all members of the BTI Targetry team.

# TABLE OF CONTENTS

|                                                                                    |            |
|------------------------------------------------------------------------------------|------------|
| <b>LIST OF TABLES</b> . . . . .                                                    | <b>vi</b>  |
| <b>LIST OF FIGURES</b> . . . . .                                                   | <b>vii</b> |
| <b>Chapter 1 Introduction</b> . . . . .                                            | <b>1</b>   |
| 1.1 Background . . . . .                                                           | 1          |
| 1.2 Purpose . . . . .                                                              | 3          |
| 1.2.1 Project Outline . . . . .                                                    | 4          |
| 1.3 Related Work . . . . .                                                         | 4          |
| <b>Chapter 2 Visualization Target Overview</b> . . . . .                           | <b>5</b>   |
| 2.1 Design . . . . .                                                               | 5          |
| 2.2 Experiment . . . . .                                                           | 7          |
| <b>Chapter 3 Computational Model of Visualization Target</b> . . . . .             | <b>8</b>   |
| 3.1 Radiation Transport via MCNPX . . . . .                                        | 8          |
| 3.2 CFD Implementation via ANSYS CFX . . . . .                                     | 10         |
| 3.2.1 Geometry and Mesh Definition . . . . .                                       | 11         |
| 3.2.2 Physics, Initial Conditions, and Boundary Conditions Specification . . . . . | 14         |
| 3.2.3 Solver . . . . .                                                             | 17         |
| 3.2.4 Results . . . . .                                                            | 19         |
| <b>Chapter 4 Coupling of Radiation Transport to Fluid Properties</b> . . . . .     | <b>24</b>  |
| 4.1 Operating Beam Current . . . . .                                               | 24         |
| 4.2 Method . . . . .                                                               | 25         |
| 4.3 Model Adaptations . . . . .                                                    | 28         |
| 4.3.1 Computational Expense . . . . .                                              | 28         |
| 4.3.2 Mesh Study . . . . .                                                         | 32         |
| 4.4 Results . . . . .                                                              | 35         |
| 4.4.1 Full Model and Iterative Model Results Comparison . . . . .                  | 36         |
| 4.4.2 Original and Iterated Beam Comparison . . . . .                              | 40         |
| 4.4.3 Experimental Validation . . . . .                                            | 42         |
| <b>Chapter 5 Conclusion</b> . . . . .                                              | <b>44</b>  |
| 5.1 Future Work . . . . .                                                          | 44         |
| <b>References</b> . . . . .                                                        | <b>46</b>  |
| <b>Appendices</b> . . . . .                                                        | <b>48</b>  |
| Appendix A . . . . .                                                               | 49         |
| Appendix B . . . . .                                                               | 51         |
| Appendix C . . . . .                                                               | 55         |

Appendix D . . . . . 60

## LIST OF TABLES

|           |                                                                                                        |    |
|-----------|--------------------------------------------------------------------------------------------------------|----|
| Table 3.1 | Domain Cell Count . . . . .                                                                            | 13 |
| Table 3.2 | Sapphire Material Properties . . . . .                                                                 | 14 |
| Table 3.3 | Domain Maximum Temperatures . . . . .                                                                  | 21 |
| Table 4.1 | Saturation Temperature Study Results . . . . .                                                         | 24 |
| Table 4.2 | Heat Transfer Coefficient Calculation Results . . . . .                                                | 30 |
| Table 4.3 | Maximum Temperature Comparison: Full Model and Applied Heat Transfer<br>Coefficient Function . . . . . | 30 |
| Table 4.4 | Full Model and Adapted Model Comparison . . . . .                                                      | 36 |
| Table 4.5 | Original Beam vs. Iterated Beam . . . . .                                                              | 40 |
| Table C.1 | Rectangle Model: Maximum Temperatures . . . . .                                                        | 56 |
| Table C.2 | Rectangle Model: Saturation Temperature Study Results . . . . .                                        | 58 |



## LIST OF FIGURES

|             |                                                                               |    |
|-------------|-------------------------------------------------------------------------------|----|
| Figure 1.1  | Bragg Peak . . . . .                                                          | 3  |
| Figure 2.1  | Visualization Target: Isometric View and Section View . . . . .               | 5  |
| Figure 2.2  | Coolant Channel Orientation . . . . .                                         | 6  |
| Figure 3.1  | Contour and Surface Plots of Gaussian Beam Distribution . . . . .             | 9  |
| Figure 3.2  | MCNPX Energy Deposition Plot . . . . .                                        | 10 |
| Figure 3.3  | Original (a) and Simplified (b) Geometries . . . . .                          | 11 |
| Figure 3.4  | Target Mesh . . . . .                                                         | 12 |
| Figure 3.5  | Mesh Boundary Layer: Target Water Chamber (a) and Coolant Channel(b) .        | 13 |
| Figure 3.6  | Beam Distributions: MCNPX (a) and ANSYS CFX (b) . . . . .                     | 20 |
| Figure 3.7  | Target Water Temperature Distribution . . . . .                               | 21 |
| Figure 3.8  | Target Body Temperature Distribution . . . . .                                | 22 |
| Figure 3.9  | Target Water Velocity Streamline . . . . .                                    | 23 |
| Figure 4.1  | MCNPX Discretization Scheme . . . . .                                         | 25 |
| Figure 4.2  | Iterative Process Flow Chart . . . . .                                        | 27 |
| Figure 4.3  | Coolant Channel Labeling Definition . . . . .                                 | 29 |
| Figure 4.4  | Target temperature profiles: Original (a) and HTC Function (b) . . . . .      | 31 |
| Figure 4.5  | Target water velocity streamlines : Original (a) and HTC Function (b) . . . . | 31 |
| Figure 4.6  | First mesh change: smaller elements . . . . .                                 | 33 |
| Figure 4.7  | Extended Boundary Layer Mesh (a) and Beam Distribution (b) . . . . .          | 34 |
| Figure 4.8  | Adapted Mesh (a) and Beam Distribution (b) . . . . .                          | 35 |
| Figure 4.9  | Density Residual Convergence Plot . . . . .                                   | 36 |
| Figure 4.10 | Full (a) and Iterative (b) Model Beam Distributions . . . . .                 | 37 |
| Figure 4.11 | Full (a) and Iterative (b) Models Target Body Temperature Distributions . .   | 38 |
| Figure 4.12 | Full (a) and Iterative (b) Models Target Water Temperature Distributions . .  | 38 |
| Figure 4.13 | Target Water Temperature Difference ( $\Delta T$ ) in $^{\circ}F$ . . . . .   | 39 |
| Figure 4.14 | Full (a) and Iterative (b) Models Target Water Velocity Streamlines . . . . . | 39 |
| Figure 4.15 | Original (a) and Iterated (b) Beam Distributions . . . . .                    | 40 |
| Figure 4.16 | Line Plot - Original and Iterated Beam Centerline . . . . .                   | 41 |
| Figure 4.17 | Original (a) and Iterated (b) Temperature Distributions . . . . .             | 42 |
| Figure 4.18 | Experimental and Computational Beams . . . . .                                | 43 |
| Figure B.1  | Momentum and Mass Residual Plot . . . . .                                     | 52 |
| Figure B.2  | Heat Transfer Residual Plot . . . . .                                         | 53 |
| Figure B.3  | Turbulence (KE) Residual Plot . . . . .                                       | 54 |
| Figure C.1  | CAD Model: Rectangular Target . . . . .                                       | 55 |
| Figure C.2  | Rectangle Model: Energy Deposition Distribution . . . . .                     | 56 |
| Figure C.3  | Rectangle Model: Target Temperature Distribution . . . . .                    | 57 |
| Figure C.4  | Rectangle Model: Target Water Temperature Distribution . . . . .              | 58 |

|            |                                                                |    |
|------------|----------------------------------------------------------------|----|
| Figure C.5 | Rectangle Model: Target Water Velocity Streamlines . . . . .   | 59 |
| Figure D.1 | CAD Model: Slant Target . . . . .                              | 60 |
| Figure D.2 | Slanted Model: Target Temperature Distribution . . . . .       | 62 |
| Figure D.3 | Slanted Model: Target Water Temperature Distribution . . . . . | 63 |
| Figure D.4 | Rectangle Model: Target Water Velocity Streamlines . . . . .   | 64 |

# Chapter 1

## Introduction

### 1.1 Background

Positron emission tomography (PET) is an in vivo medical imaging modality that utilizes a radiolabeled molecule to track biochemical processes. Commonly used nuclides are  $^{11}\text{C}$ ,  $^{13}\text{N}$ ,  $^{15}\text{O}$ , and  $^{18}\text{F}$ .  $^{18}\text{F}$ -deoxyglucose (FDG) is a radiolabeled sugar analog synthesized from  $^{18}\text{F}$ . FDG is the primary radiopharmaceutical used in PET. Approximately 97% of  $^{18}\text{F}$  decay is by positron ( $\beta^+$ ) emission.  $^{18}\text{F}$  is an effective imaging tool because positron annihilation produces two coincident 511-keV annihilation photons that travel in opposite directions ( $180^\circ$ ). Coincidence detectors determine the location of the positron annihilation to track FDG as it is metabolically trapped in the body. Cancer cells are characterized as being very metabolically active, so an increased concentration of FDG is trapped in these cells. The increased positron annihilation in these areas allows an image to be constructed from the coincident detector signals.

$^{18}\text{F}$  has a half-life of approximately 110 minutes, so it must be made to order by a radio-pharmacy, synthesized into FDG, and transported to test sites within a few hundred miles [12]. The typical method of producing  $^{18}\text{F}$  is a (p,n) reaction with  $^{18}\text{O}$  enriched water ( $\text{H}_2^{18}\text{O}$ ). It is most commonly made with a batch-style target attached to a cyclotron. The cross section for this reaction implies that a large number of incident protons are required to create the de-

sired amount of the radioisotope. This generates a significant amount of heat within the target medium, so the main focus for target design is heat removal capability.

A proton deposits energy via collisions as it travels through the water. The average amount of energy lost per unit length as a charged particle travels through a medium is called the stopping power. Stopping power is most commonly used in the units MeV cm<sup>-1</sup> and is represented by the term  $-\frac{dE}{dx}$  [14]. The stopping power of a proton is given by the Bethe Formula for Stopping Power (Equation 1.1).

$$-\frac{dE}{dx} = \frac{4\pi k_0^2 z^2 e^4 n}{mc^2 \beta^2} \left[ \ln \frac{2mc^2 \beta^2}{I(1 - \beta^2)} - \beta^2 \right] \quad (1.1)$$

where:

$k_0 = 8.99 \times 10^9 \text{ N m}^2\text{C}^{-2}$ ,

$z =$  atomic number of the charge particle,

$e =$  magnitude of the electron charge,

$n =$  number of electrons per unit volume in the medium,

$m =$  electron rest mass,

$c =$  speed of light in vacuum,

$\beta = \frac{V}{c} =$  speed of the particle relative to  $c$ ,

$I =$  mean excitation energy of the medium.

As the the energy of the particle approaches zero,  $\beta$  approaches zero. The logarithmic term decreases, causing an increase in the stopping power called the Bragg Peak [14] (shown for 18 MeV protons in water in Figure 1.1). The distance traveled per unit energy of the proton is found by taking the reciprocal of the stopping power. Using this, the range of a particle of kinetic energy  $T$  can be found using Equation 1.2:

$$R(T) = \int_0^T \left(-\frac{dE}{dx}\right)^{-1} dE. \quad (1.2)$$

BTI Targetry LLC partnered with North Carolina State University in 2000 to model the

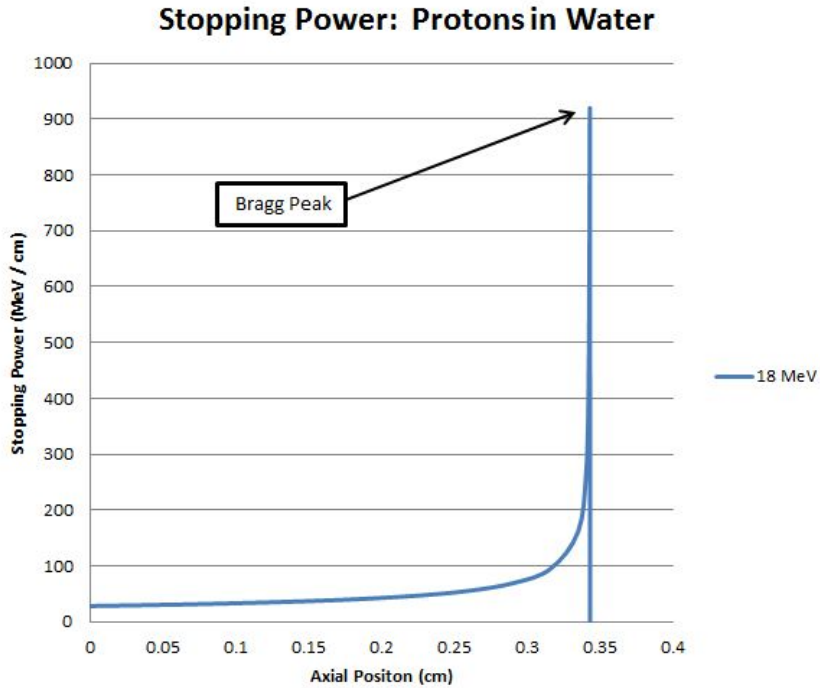


Figure 1.1: Bragg Peak

heat transfer capabilities of various cyclotron targets using Monte Carlo Radiation Transport and Computational Fluid Dynamics (CFD) software. All previous modeling for boiling water targets has been done using assumptions for the distribution of void under saturation conditions [11]. To investigate void distribution, BTI Targetry developed a visualization target that would allow video recording of the target chamber during irradiation. The target was sufficiently robust to operate under conditions that are consistent with typical  $^{18}\text{F}$  production targets.

## 1.2 Purpose

The purpose of this work is to construct a computational model for the heat transfer of the primary target fluid with coupling between radiation transport and fluid properties. As previously discussed, the range of charged particles is dependent on the particle energy and the density of

the medium. As the target water is heated by the energy deposition from the proton beam, a non-uniform density distribution develops within the target water. As the location of highest temperature should be located at the Bragg peak of the proton beam, it is expected that the fluctuation of the density at this point will affect the range of protons. This effect on the range will be magnified when the target water transitions from single phase liquid to boiling. The scope of this project is to couple the energy deposition profiles computed with the MCNPX radiation transport code with the fluid density distribution from ANSYS CFX for a target with single phase liquid. The beam current was kept at a level that did not result in temperatures exceeding the saturation temperature at the operating pressure.

### **1.2.1 Project Outline**

First, an initial computational model was developed to provide a solution that offered acceptable agreement with the experimental results. This initial model and corresponding results are discussed in Chapter 3. After the analysis of these results, several adaptations were made to the initial model to improve resolution and computational expense that would allow for this model to be used as an iterative step within an algorithm that couples the beam data to the fluid results. These adaptations to the initial model and the results from the iterative method are presented in Chapter 4.

## **1.3 Related Work**

BTI Targetry, LLC (formerly Bruce Technologies, Inc.) has been developing computational models of water targets for several years. They have computationally modeled both batch-style and recirculating target systems, but have not previously linked the radiation transport information to the fluid property distributions provided by CFD software. Other research has been done on a visualization target system [6], [7], but all work was strictly experimental with no computational modeling.

## Chapter 2

# Visualization Target Overview

In this section, the design of the visualization target is examined. All design work and experimentation was completed by BTI Targetry, LLC.

### 2.1 Design

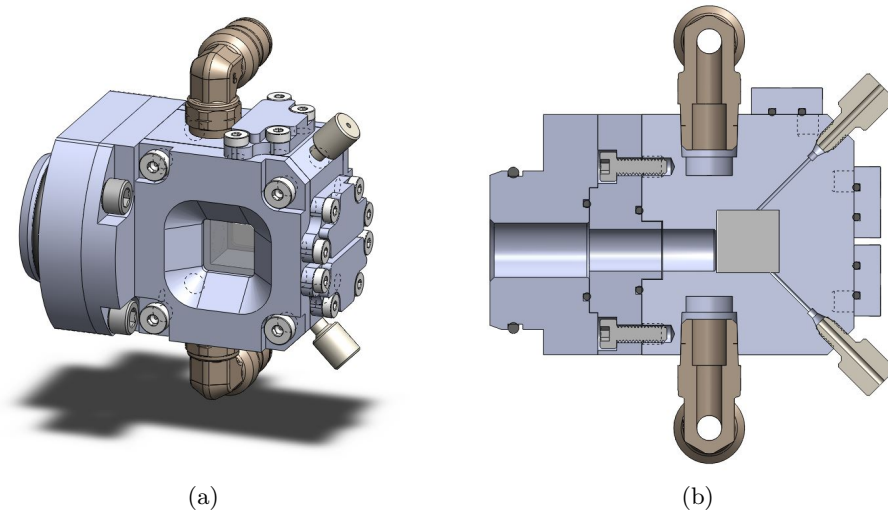


Figure 2.1: Visualization Target: Isometric View and Section View

The visualization target water chamber was designed to have a similar volume to a typical production target chamber. The target water chamber dimensions are  $14 \times 15 \times 15$  mm (max fill volume of 3.15 mL). The 0.005 inch beam window is integrated into the target body and there are two viewing windows.

The visualization target must operate at the same range of particle energies and beam currents as current production targets. This required material choices with similar thermal properties and a cooling system capable of removing the heat deposited by the proton beam. The target body is made of Aluminum 6061-T because it is a low cost, machinable metal with thermal conductivity that allows for adequate heat transfer. For the viewing windows, optically clear sapphire ( $\text{Al}_2\text{O}_3$ ) was chosen for its ability to withstand the operating pressures as well as significantly higher thermal conductivity when compared to standard glass. The cooling system uses liquid water pumped through a system of cooling channels through the target body. The

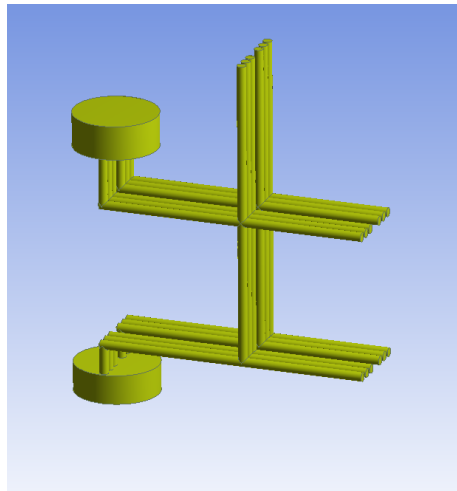


Figure 2.2: Coolant Channel Orientation

coolant flows into the top of the target chamber and passes into the target body where it flows into six coolant channels that flow around three sides of the target water chamber before exiting



the target body. Figure 2.2 is an image of the coolant channel orientation as described above. There are three extensions from the coolant channels into the target body that were necessary because of the machining techniques used to fabricate the target. These channels extensions are closed by flanges and are not active flow channel inlets or outlets.

## **2.2 Experiment**

The visualization target was used on an IBA Cyclone 18/9 cyclotron [3] with a 10 mm beam collimation diameter with power ratings up to 1.1 kW. The target chamber was filled with 2.5 mL of water with helium gas filling the rest of the target chamber volume. The target was operated over a range of pressures and beam currents. Natural convection within the target water was observed for both single and two phase flow. The beam penetration depth and Bragg peak location were also visible under different lighting conditions due to de-excitation photons from the water[10].

## Chapter 3

# Computational Model of Visualization Target

A computational model was developed for the visualization target. This model was developed as a simple, initial solution to be compared against the experimental results to validate the effectiveness of MCNPX beam data applied as a heat source within a CFD model.

### 3.1 Radiation Transport via MCNPX

MCNPX is a Monte Carlo radiation transport code provided by the Department of Energy that models particle interaction. This program was used to create energy deposition data tallies from proton interaction with the target water and the aluminum beam window. MCNPX generates this data from an input file that defines the domains, materials, material properties, particle type, particle energy, and beam radius [2].

The visualization target operated with a 10 mm diameter beam collimation (5 mm radius). The MCNPX beam definition requires a full width at half maximum (FWHM) for the beam at a specified transmission. The FWHM in two dimensions ( $x$  and  $y$ ) can be calculated using Equations 3.1 and 3.2 with  $\sigma_x$  and  $\sigma_y$  being the standard deviations in the  $x$  and  $y$  directions.

$$f_x = 2\sqrt{2 \ln 2} \sigma_x \quad (3.1)$$

$$f_y = 2\sqrt{2 \ln 2} \sigma_y \quad (3.2)$$

The beam was modeled with a 50% transmission for 18 MeV protons. The FWHM for the desired transmission percentage and beam radius was calculated with a MATLAB code that integrated over the Gaussian distribution function with increasing  $\sigma_x$  and  $\sigma_y$  until the transmission percentage reached the desired amount (50%). This integration is shown in Equation 3.3.

$$\int_0^{2\pi} \int_0^5 \frac{1}{2\pi\sigma_x\sigma_y} e^{-\left(\frac{r \cos \theta}{2\sigma_x^2} + \frac{r \sin \theta}{2\sigma_y^2}\right)^2} r dr d\theta \quad (3.3)$$

$\sigma_x$  and  $\sigma_y$  were found to be 4.2410 mm for 50% transmission, yielding a FWHM of 9.9868 mm for both the  $x$  and  $y$  directions. A two and three-dimensional plot of the Gaussian beam distribution is shown in Figure 3.1. A representative plot of the proton energy deposition tally

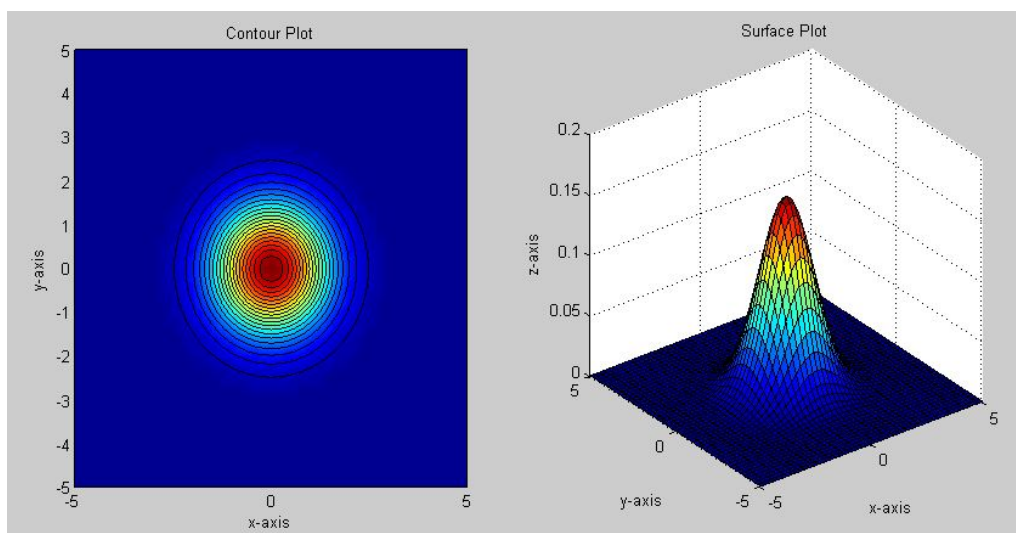


Figure 3.1: Contour and Surface Plots of Gaussian Beam Distribution

is shown in Figure 3.2. The scale is relative to energy deposition.

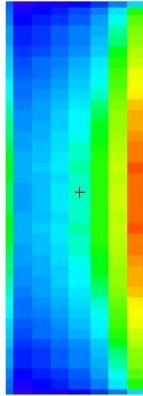


Figure 3.2: MCNPX Energy Deposition Plot

A target geometry is created within an MCNPX model via specified planes that serve as boundaries. Each domain space is identified by the plane boundaries that surround it. The material definition for that cell is specified by the chemical formula for the material and user specified density. For this beam model, the beam window and target water were specified as cylinders since the beam collimator projects the beam in a cylindrical shape through the beam window and target water. For the initial calculations, a uniform density was applied to the water domain for the energy deposition calculations.

### 3.2 CFD Implementation via ANSYS CFX

ANSYS CFX is a CFD software package capable of modeling fluid flow and heat transfer for solid and fluid domains. It includes four software modules that pass information required for the model analysis. The modeling process has four basic phases:

1. Geometry and Mesh definition

2. Physics, Initial Conditions, and Boundary Conditions Specification
3. Solver
4. Post-Processing the Results from the Solver

### 3.2.1 Geometry and Mesh Definition

#### Geometry

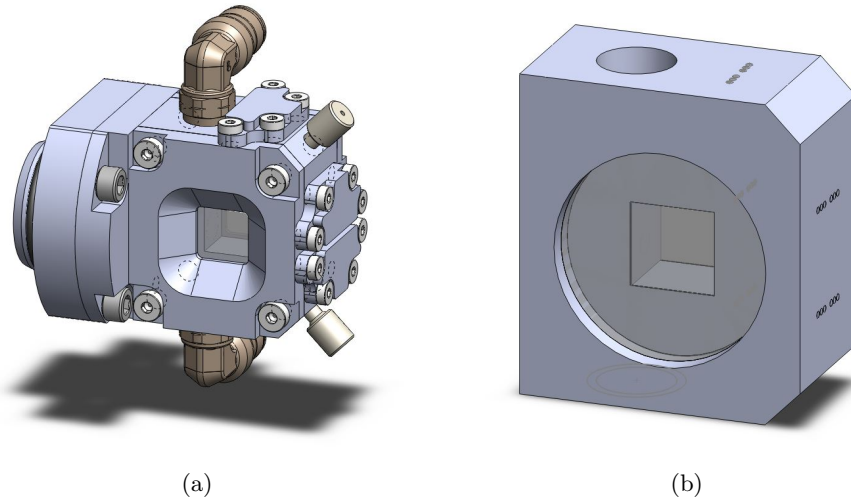


Figure 3.3: Original (a) and Simplified (b) Geometries

ANSYS CFX has built-in geometry generation software that is capable of importing geometry files from other sources. A CAD model of the visualization target created in SolidWorks was provided. This model was fully detailed for fabrication, so the computational model for this study used a simplified version of the provided geometry to manage computational expense. The external flanges, coolant and target water input ports, and all threading, fasteners, and o-rings were removed to simplify the geometry. Shown in Figure 3.3 are the original and simplified

versions of the CAD model used in this study (view of the simplified geometry magnified).

### Mesh Definition

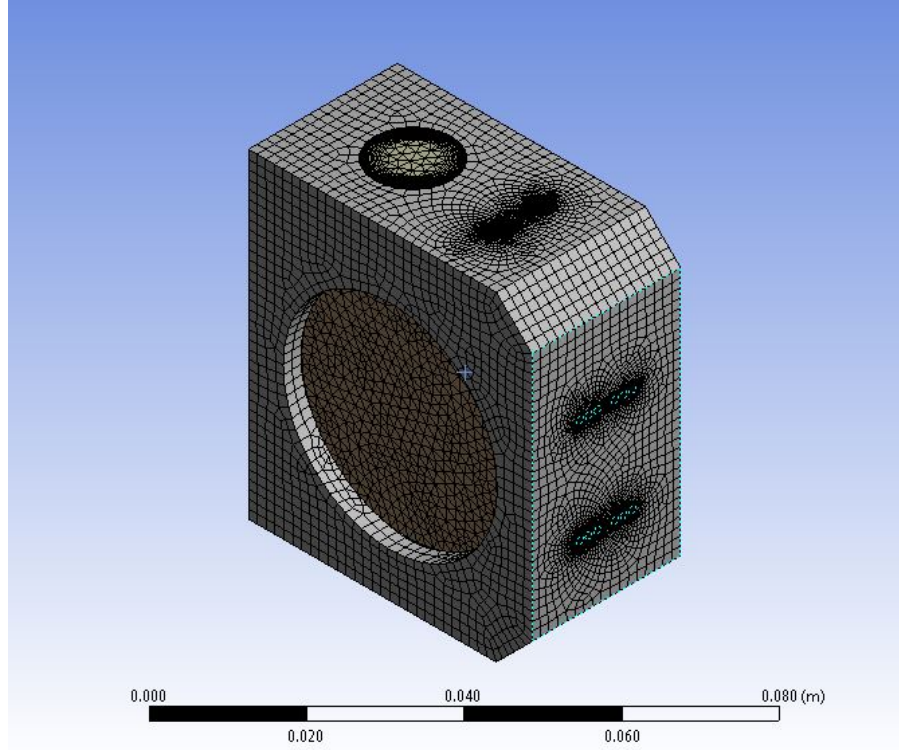


Figure 3.4: Target Mesh

Each domain within the geometry can have a different meshing scheme. The target body was meshed with hexagonal elements, as it is effective for solid domains with large amounts of interior volume. The other solid domains and liquid domains are meshed with the patch-conforming method with tetrahedral elements. This method allows for three-dimensional inflation that develops the boundary layer necessary to resolve near-wall velocity profiles. The meshing scheme for the visualization target is shown in Figure 3.4. Table 3.1 gives the total

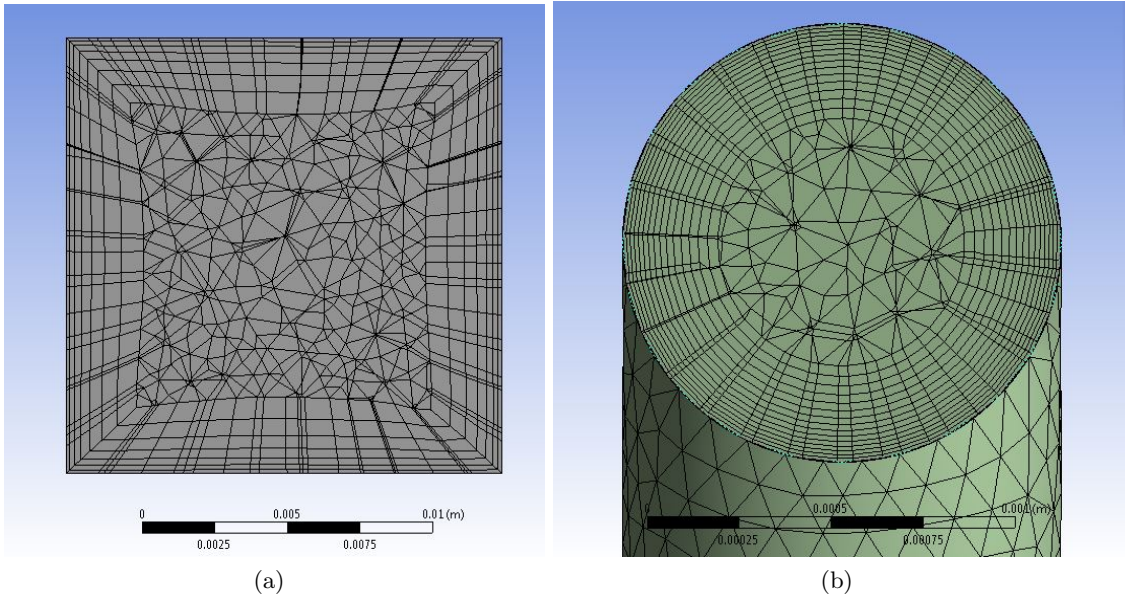


Figure 3.5: Mesh Boundary Layer: Target Water Chamber (a) and Coolant Channel(b)

Table 3.1: Domain Cell Count

| Domain           | Cell Total |
|------------------|------------|
| Target           | 1,384,171  |
| Target Water     | 33,710     |
| Coolant          | 3,149,234  |
| Sapphire Windows | 14,776     |

number of cells within each computational domain.

The boundary layer of the liquid region mesh should allow for a smooth transition from a zero wall velocity to the fully developed bulk velocity. To properly develop the boundary layer, the wall boundary element must be within the laminar sublayer of the fluid. The  $y^+$  value of a mesh is a dimensionless number that expresses the distance from the boundary to the center of the first computational node [1]. This value is a function of the fluid velocity as well as the element size, and calculated with Equation 3.4:

$$y^+ = \frac{u_* \cdot y}{\nu} \quad (3.4)$$

where

$$u_* = \sqrt{\frac{\tau_w}{\rho}} \quad (3.5)$$

A  $y^+ < 11$  places the first element within the viscous sub-layer region of the fluid [9]. This is critical for proper resolution in areas where the near wall velocities and temperatures are being analyzed. The mesh for the target water chamber was meshed with a maximum  $y^+$  value of approximately 3, allowing full resolution of the wall boundaries. The mesh scheme for the target water chamber and the coolant channel for this phase of the study is shown in Figure 3.5.

### 3.2.2 Physics, Initial Conditions, and Boundary Conditions Specification

#### Material Specifications

The target body material specification was for the default aluminum values provided in the ANSYS CFX material libraries. Both the coolant and target water were specified as liquid water, with fluid properties provided from a table as a function of current temperature and pressure. Sapphire was not provided within the material library, so a material was defined. The properties required for the material specification and their respective values are provided in Table 3.2 [5].

Table 3.2: Sapphire Material Properties

|                      |                                      |
|----------------------|--------------------------------------|
| Chemical Formula     | $\text{Al}_2\text{O}_3$              |
| Density              | $3.98 \text{ g cm}^{-3}$             |
| Specific Heat        | $761 \text{ J kg}^{-1}\text{K}^{-1}$ |
| Thermal Conductivity | $23.1 \text{ W m}^{-1}\text{K}^{-1}$ |



## Initial and Boundary Conditions

The initial temperature specification of the solid domains is 60° F. The exterior boundaries of the target are set to adiabatic for heat transfer. The exterior boundaries of the physical target are within the vacuum chamber of the cyclotron, so only radiative heat transfer is physically valid. The amount of heat transferred from the target via this method is negligible compared to the heat removed from the target via the coolant, so an adiabatic specification for these boundaries is within an acceptable amount of error. The boundary condition between the fluid domains and the solid domains are set as a no slip wall condition. This gives a zero fluid velocity at the wall boundary. The heat transfer mechanism between the fluid and solid domains is conjugate heat transfer with no contact resistance. This allows for calculation of heat flux via the convective heat transfer mechanism. The boundaries between the sapphire windows and the aluminum target body are set as a domain interface with calculation of heat transfer via conduction between the two materials. A contact resistance of  $900 \text{ W m}^{-2} \text{ K}^{-1}$  was applied to the domain interfaces between the sapphire and aluminum domains [13].

Both the coolant and target water are initially set to 60° F at an operating pressure of 400 psia. The inlet boundary for the coolant channel was set to 60° F with a mass flow of  $0.06309 \text{ kg s}^{-2}$  ( $1 \text{ gal min}^{-1}$ ). The exit boundary of the coolant channel was set for an average static pressure of 400 psia. These values were chosen based on the operating conditions for targets used for commercial production of  $^{18}\text{F}$ . The ends of the coolant channels that are blocked by flanges in the visualization target were modeled as adiabatic, no slip walls. It was expected that the majority of the heat transfer from the target body in the the coolant channels would take place in the areas closest to the target water chamber with a negligible amount occurring at the ends of the coolant channel extension. This justifies the adiabatic specification for these boundaries.

## Turbulence Model

While the Navier-Stokes equations are theoretically capable of solving the laminar and turbulent flow regions, the computational expense necessary to resolve these regions is so high that current computational capabilities are inadequate [1]. Instead, various turbulence models have been created to resolve the effects of turbulence on fluid flow. The most popular turbulence models are characterized as two-equation models. ANSYS CFX only allows for one turbulence model to be used within a single computational model, so a turbulence model that was capable of solving for the fluid flow within the target water chamber and the coolant channels was necessary.

The standard k- $\epsilon$  model was chosen for this study [8]. It is an accurate, robust model that is applicable for the majority of flow situations. The k- $\epsilon$  model introduces two new variables: k and  $\epsilon$  [1]. These variables come from the differential transport equations for turbulence kinetic energy and turbulence dissipation rate, given in Equation 3.6 and 3.7, where k is the turbulent kinetic energy with units  $\text{m}^2 \text{s}^{-2}$  and  $\epsilon$  is the eddy dissipation with units  $\text{m}^2 \text{s}^{-3}$ .

$$\frac{\delta(\rho k)}{\delta t} + \frac{\delta}{\delta x_j}(\rho U_j k) = \frac{\delta}{\delta x_j}[(\mu + \frac{\mu_t}{\sigma_k})\frac{\delta k}{\delta x_j}] + P_k - \rho\epsilon + P_{kb} \quad (3.6)$$

$$\frac{\delta(\rho\epsilon)}{\delta t} + \frac{\delta}{\delta x_j}(\rho U_j \epsilon) = \frac{\delta}{\delta x_j}[(\mu + \frac{\mu_t}{\sigma_\epsilon})\frac{\delta\epsilon}{\delta x_j}] + \frac{\epsilon}{k}(C_{\epsilon 1}P_k - C_{\epsilon 2}\rho\epsilon + C_{\epsilon 1}P_{\epsilon b}) \quad (3.7)$$

$C_{\epsilon 1}$ ,  $C_{\epsilon 2}$ ,  $\sigma_k$ , and  $\sigma_\epsilon$  are constants,  $P_{kb}$  and  $P_{\epsilon b}$  are the buoyancy force influences, and  $P_k$  is the turbulence production from viscous forces. This model is used to solve for the turbulent viscosity, given by Equation 3.8.

$$\mu_t = C_\mu \rho \frac{k^2}{\epsilon} \quad (3.8)$$

The standard k- $\epsilon$  model is valid for  $y^+ > 30$  [8]. However, this does not allow for sufficient resolution of the near-wall region. ANSYS CFX uses an adaptive scalable wall function approximation in areas where the boundary layer yields a  $y^+ < 30$  [1]. This provides a consistent solution in areas with variable  $y^+$  values, and is useful in areas where visualization of the details

of the boundary layer are important. Properly resolving the boundary layers within the coolant channels proved to be computationally very expensive, as the channels have physically small diameters (1 mm). For this reason, the mesh chosen for the coolant channels was allowed to have a  $y^+ > 30$ . The boundary layer definition within the coolant channels (shown in Figure 3.5) was sufficient to provide a convergent solution, and kept computational costs down.

### Proton Beam Data

The proton beam data is input into ANSYS CFX using a three-dimensional interpolation function. MCNPX outputs a tally sheet with heat generation rates over a specified set of cells expressed in cylindrical coordinates. A FORTRAN code was written to translate the tally output from MCNPX for a specified beam current into a three-dimensional pointwise heat generation table in Cartesian coordinates. These points can be imported into ANSYS CFX, which then calculates an interpolation function that is applied to the beam window and target water. This interpolation function is included in the solution stage as an energy source. This interpolation function can be view in the post-processor as a distribution by specifying a variable within the set-up that tracks the nodal values of the interpolation function.

### 3.2.3 Solver

CFD software packages solve the Navier-Stokes equations to model heat transfer, fluid flow, and other physical processes for specified domains and boundary conditions. ANSYS CFX uses the Finite Element Method (FEM) to solve the unsteady Navier-Stokes equations in conservative form. The non-linear equations are linearized and are then solved by an Algebraic Multigrid solver[4]. The instantaneous mass, momentum, and energy conservation equations are given by Equations 3.9-3.15 [1]:

$$\frac{\delta\rho}{\delta t} + \nabla \cdot (\rho\mathbf{U}) = 0 \tag{3.9}$$

$$\frac{\delta(\rho \mathbf{U})}{\delta t} + \nabla \cdot (\rho \mathbf{U} \otimes \mathbf{U}) = -\nabla p + \nabla \cdot (\mu(\nabla \mathbf{U} + (\nabla \mathbf{U}^T - \frac{2}{3}\delta \nabla \cdot \mathbf{U}))) + \mathbf{S}_M \quad (3.10)$$

$$\frac{\delta(\rho h_{tot})}{\delta t} - \frac{\delta p}{\delta t} + \nabla \cdot (\rho \mathbf{U} h_{tot}) = \nabla \cdot (\lambda \nabla T) + \nabla \cdot (\mathbf{U} \cdot \boldsymbol{\tau}) + \mathbf{U} \cdot \mathbf{S}_M + \mathbf{S}_E \quad (3.11)$$

where  $\nabla \cdot (\mathbf{U} \cdot \boldsymbol{\tau})$  is the viscous work term,  $\mathbf{U} \cdot \mathbf{S}_M$  is the external momentum source work term, and  $\mathbf{S}_E$  is the external energy source term. The total enthalpy ( $h_{tot}$ ) is related to the static enthalpy ( $h(T, P)$ ) by Equation 3.12:

$$h_{tot} = h + \frac{1}{2} \mathbf{U}^2 \quad (3.12)$$

Applying the k- $\epsilon$  model gives the new set of Navier-Stokes equations:

$$\frac{\delta \rho}{\delta t} + \frac{\delta}{\delta x_j} (\rho U_j) = 0 \quad (3.13)$$

$$\frac{\delta \rho U_i}{\delta t} + \frac{\delta}{\delta x_j} (\rho U_i U_j) = -\frac{\delta p'}{\delta x_i} + \frac{\delta}{\delta x_j} [\mu_{eff} (\frac{\delta U_i}{\delta x_j} + \frac{\delta U_j}{\delta x_i})] + S_M \quad (3.14)$$

$$\frac{\delta(\rho h_{tot})}{\delta t} - \frac{\delta p}{\delta t} + \nabla \cdot (\rho \mathbf{U} h_{tot}) = \nabla \cdot (\lambda \nabla T + \frac{\mu_t}{Pr_t} \nabla h) + \nabla \cdot (\mathbf{U} \cdot \boldsymbol{\tau}) + \mathbf{U} \cdot \mathbf{S}_M + \mathbf{S}_E \quad (3.15)$$

where  $\mu_{eff}$  is the effective viscosity given by Equation 3.16 ( $\mu_t$  defined in Equation 3.8), and  $p'$  is the modified pressure given by Equation 3.17.

$$\mu_{eff} = \mu + \mu_t \quad (3.16)$$

$$p' = p + \frac{2}{3}\rho k + \frac{2}{3}\mu_{eff} \frac{\delta U_k}{\delta x_k} \quad (3.17)$$

The above equations have no general analytic solution, requiring a iterative numerical solution. The equations are discretized and solved numerically using FEM to calculate the mass, momentum, energy, and turbulence variables. These solutions are iterated upon until a user selected convergence criteria has been met. The default value for convergence is set for a relative L<sup>2</sup> norm, Root Mean Squared (RMS), residual (Equation 3.18) at 1 e -4 in ANSYS CFX. This value is used as the primary residual value goal used in this study. An example residual convergence plot is given in the Appendix.

$$\| x \|_2 = \left( \sum_{i=1}^n | x_i |^2 \right)^{\frac{1}{2}} \quad (3.18)$$

### 3.2.4 Results

The computational model for the visualization target with a 10 $\mu$ A beam of 18 MeV protons (180 W total energy input) with the settings described above was run with 8 partitions on 8 Intel Xeon Processors computational cores on the Henry 2 cluster. It took approximately 72 hours to reach the default convergence criteria 1e-4.

#### Proton Beam Energy Deposition

The proton beam deposits 10.54 W into the beam window and 169.46 W into the target water for a total of 180 W. The overall distribution was very similar to the energy deposition plot created within MCNPX. There are differences between the two models because of the different cell shapes assumed in MCNPX and ANSYS CFX (see Figure 3.6). Note that the scale within Figure 3.6 have different units and magnitudes. Also note that MCNPX plots a zero value as white, while ANSYS CFX plots a zero value as dark blue. The location of the Bragg peak is poorly resolved with the ANSYS CFX scheme compared to the MCNPX discretization, but the overall heat input over the target was accurate. Better resolution of the beam distribution

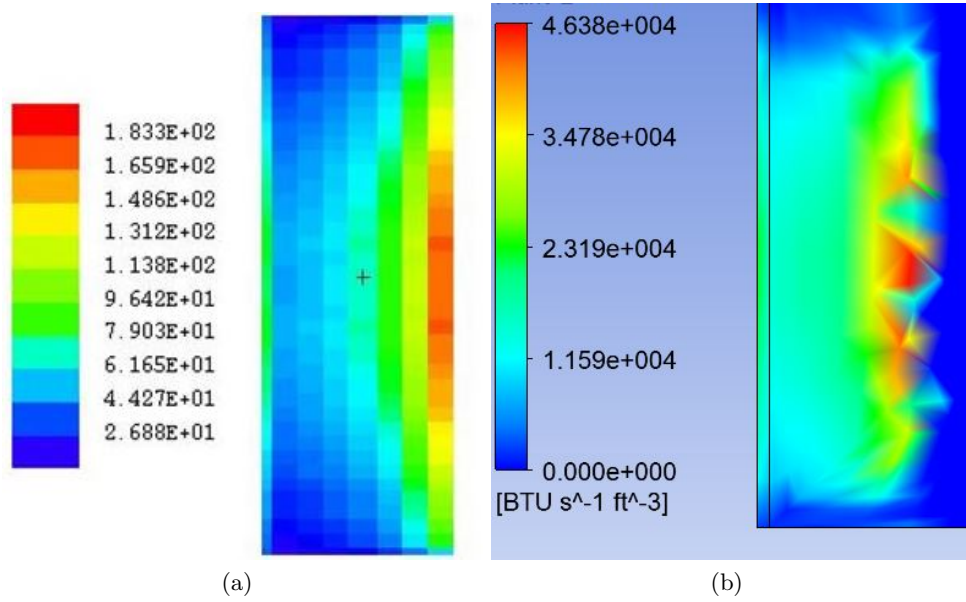


Figure 3.6: Beam Distributions: MCNPX (a) and ANSYS CFX (b)

could be achieved by reducing the mesh element size within ANSYS CFX. However, this would increase the computational costs of the model. At this phase of the study, a precise resolution and location of the Bragg peak was not critical, so this mesh was sufficient. However, the mesh was refined for later phases of the study.

### Temperature

The maximum temperature computed within the model is found just above the top of the Bragg peak in the target water, shown in Figure 3.7. The maximum temperature in the target body is located at the center of the beam strike in the target window. The maximum temperatures for each domain is listed in Table 3.3.

The majority of the target body is approximately 60° F. The areas with the largest temperature increases are just above and below the beam port. The bulk of the heat from the target water is transferred through the top of the target into the coolant channels. The target water cooling as it rises out of the beam strike area causes natural circulation currents to develop.

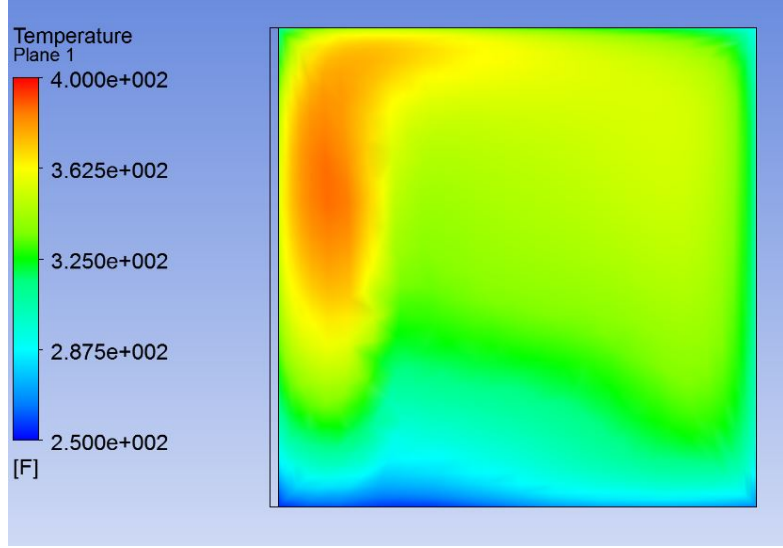


Figure 3.7: Target Water Temperature Distribution

Table 3.3: Domain Maximum Temperatures

| Domain           | Temperature ( $^{\circ}$ F) |
|------------------|-----------------------------|
| Target Water     | 387.58                      |
| Target           | 141.48                      |
| Sapphire Windows | 334.77                      |
| Coolant          | 63.27                       |

### Velocity

The velocity profiles within the target water clearly shows the natural circulation currents developing within the target water chamber (Figure 3.9). The maximum velocity within the target water is approximately  $5.4 \text{ cm s}^{-1}$ . The maximum velocity is also located just above the Bragg peak. The buoyancy forces are the greatest at this point because of temperature difference between this area and the surrounding target water. The two other locations of relatively higher velocities are along the top and back walls of the target chamber. These are two of the cooled

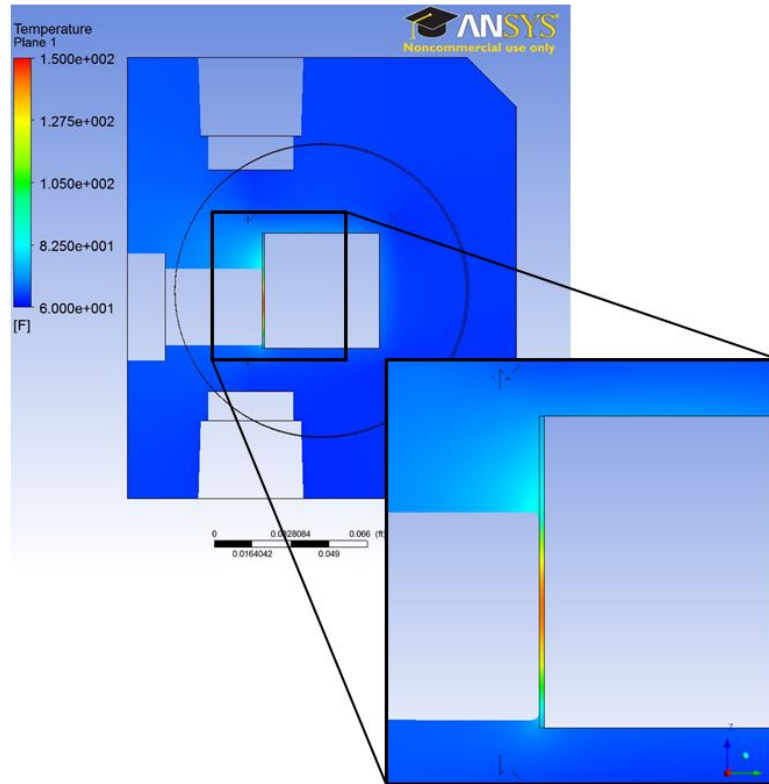


Figure 3.8: Target Body Temperature Distribution

surfaces, so the target water rapidly cools when contacting these surfaces, causing the high velocity across and down the back walls of the target chamber.



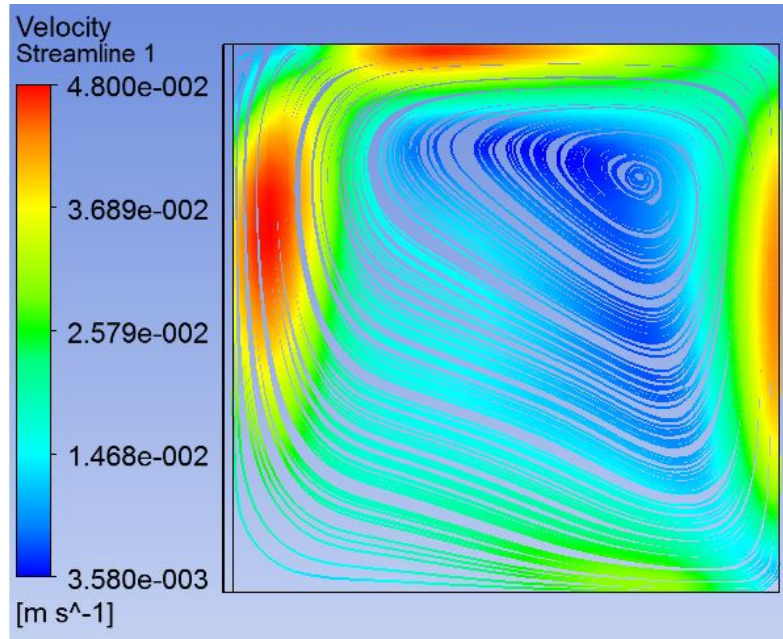


Figure 3.9: Target Water Velocity Streamline

## Chapter 4

# Coupling of Radiation Transport to Fluid Properties

### 4.1 Operating Beam Current

The first step in coupling the beam data to the fluid properties was to select an operating beam current. The beam current selection required a large enough margin between the maximum fluid temperature in the target water domain and the saturation temperature at the operating pressure.

Table 4.1: Saturation Temperature Study Results

| Beam Current ( $\mu\text{A}$ ) | Maximum Temperature ( $^{\circ}\text{F}$ ) |
|--------------------------------|--------------------------------------------|
| 10                             | 387.581                                    |
| 13                             | 427.369                                    |
| 14                             | 441.147                                    |
| 15                             | 457.141                                    |
| Saturation Temperature         | 444.616                                    |

This is critical because ANSYS CFX does not model the transition from single phase liquid into boiling. Any temperatures above the saturation temperature would result in the model no longer being physically valid.

Using the computational model, a study was done to find the minimum beam current at the selected operating conditions that results in temperatures above the saturation temperature. The results are shown in Table 4.1. The model ceases to be valid between  $14 \mu\text{A}$  and  $15 \mu\text{A}$ . Rather than operate at the highest possible beam current,  $10 \mu\text{A}$  was chosen as the operating temperature to reduce the risk of the new beam data causing the fluid temperatures to exceed the saturation temperature. Experimental results confirm that boiling does not occur at  $10 \mu\text{A}$  for the visualization target operated at 300 psi, giving confidence that this is an appropriate choice for a beam current selection.

## 4.2 Method

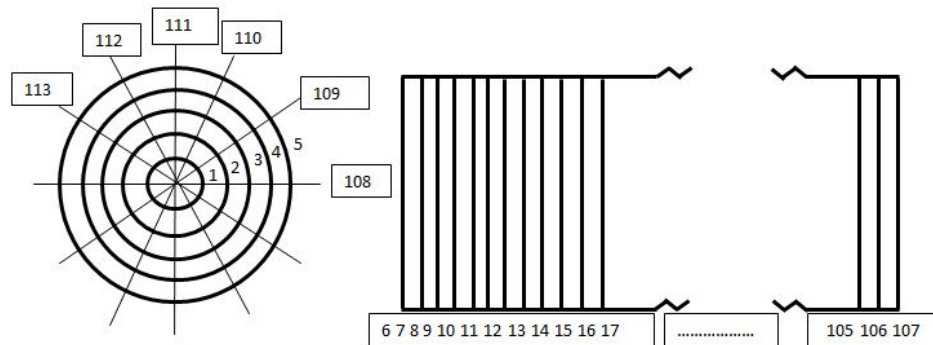


Figure 4.1: MCNPX Discretization Scheme

To improve the accuracy of the computational model, the energy deposition distribution from MCNPX must be linked to the fluid property distribution produced within ANSYS CFX. To do this, the fluid model within MCNPX must be discretized and the density distribution

applied from the CFD results. While there is an energy deposition mesh tool within MCNPX, it does not discretize the material so there is no way to apply a different material definition within each of the deposition cells. To discretize the model, a series of planes were specified and labeled within the MCNPX input card. The target water domain was discretized radially with 5 planes, axially with 100 planes, and angularly with 12 planes resulting in 6000 individual cells within the target water domain (shown in Figure 4.1).

Each discretization cell was created by referencing the planes that formed the boundaries, and required a line within the input file specifying the cell boundaries and material definition. A FORTRAN code was written to automatically write the input text file for MCNPX. This method allowed for a different density to be applied to each individual cell, but maintain the other material properties.

Applying the density distribution from the CFD results required exporting the results from ANSYS CFX. The export format for the density distribution gave a three-dimensional point-wise density distribution. The three-dimensional points are the coordinates of the nodes of the mesh elements within ANSYS CFX. These coordinates do not coincide with the centroids of the cells within the new MCNPX discretization. To interpolate the density distribution from the CFD results, the built-in three-dimensional interpolation tool *griddata3* within MATLAB was used to produce an interpolation function from the point-wise density distribution. This interpolation function was applied to the three-dimensional coordinates of the centroids of the MCNPX discretization to find the centroid density for each cell. These densities are applied to each cell via the FORTRAN code.

When the density is applied to the beam discretization, the beam shape and penetration depth changes. When this new beam data is applied to the CFD model, the density distribution changes. This density distribution can then be re-applied to the MCNPX discretization, creating an iterative process to be repeated until the density distribution and beam shape converge. A flow chart of this iterative process is shown in Figure 4.2.

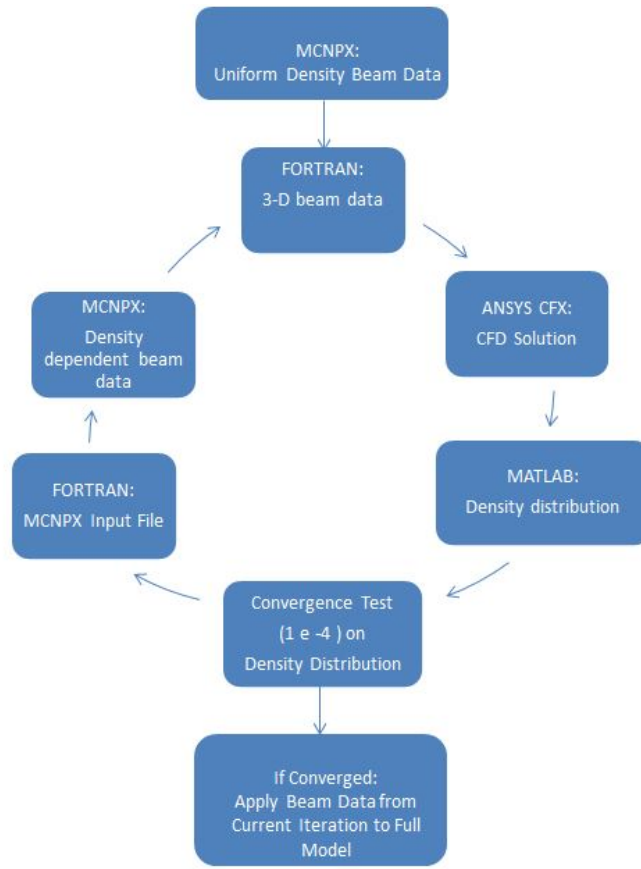


Figure 4.2: Iterative Process Flow Chart

## 4.3 Model Adaptations

For the iterative method describe to be successful, several changes had to be made to the original model. These included reducing the computational expense of the model and changing the mesh for better resolution in the beam area.

### 4.3.1 Computational Expense

Another issue with the iterative process is the amount of computational time required for a converged CFD solution of the model. The solution to the fluid flow through the coolant channels was the largest factor in the computational expense of the model. Various methods were investigated to decouple the solution to the fluid flow through the coolant channels.

#### Calculated Heat Transfer Coefficient

The first method of decoupling the coolant solution from the rest of the model was to remove the fluid domain from the model and apply a calculated heat transfer coefficient as a heat flux boundary condition. The Dittus-Boelter Correlation for flow in a smooth channel when the fluid is being heated was used for this calculation, and is given by Equation 4.1,

$$h_c = \frac{k}{d} \cdot 0.023 \cdot Re^{0.8} \cdot Pr^{0.4} \quad (4.1)$$

where  $h_c$  is the heat transfer coefficient,  $k$  is the thermal conductivity of the water,  $d$  is the diameter of the channel,  $Re$  is the Reynolds number, and  $Pr$  is the Prandtl number. The CFD solution data for the coolant fluid flow was used to find the mass flow rate through each of the channels. This mass flow rate was used in the calculation of each of the coolant channels. The coolant channels were numbered from 1 to 6, with channel 1 being the left-most channel is facing into the beam (see Figure 4.3).

Table 4.2 shows the calculated value for the convective heat transfer coefficient for each of the six channels. These heat transfer coefficients were applied to the respective coolant channel

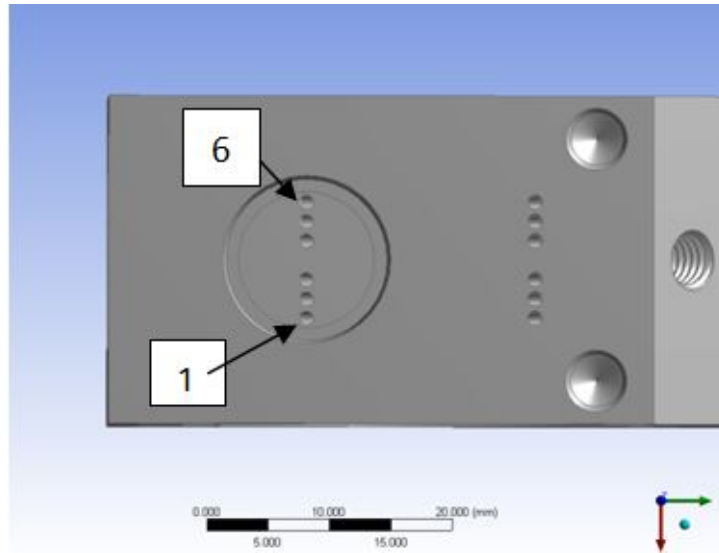


Figure 4.3: Coolant Channel Labeling Definition

boundaries with an ambient coolant temperature set to 61 °F. This method reduced the time for an ANSYS run from 72 hours partitioned on 8 parallel cores to 5 hours on a 4 core machine run serially. However, the maximum temperatures within the target water were well above the saturation temperature. Applying an average calculated heat transfer coefficient to the entire channel was not successful in maintaining the desired agreement with the full model results, so a more accurate method had to be developed.

### **Heat Transfer Coefficient Interpolation Function**

ANSYS CFX is capable of exporting point-wise solution data at the coordinates of each of the computational mesh nodes for any variable that is part of the solution. Rather than applying an average heat transfer coefficient to the entire coolant channel boundary condition, the heat transfer coefficient from the full model solution was imported into the new model setup as an interpolation function using the same method as the proton beam data. This interpolation function for the value of the heat transfer coefficient was applied to the coolant channel walls as a boundary condition with an ambient coolant temperature set to 61 °F.

Table 4.2: Heat Transfer Coefficient Calculation Results

| Channel | Mass Flux ( $\times 10^6$ )<br>(lb hr <sup>-1</sup> ft <sup>-2</sup> ) | Re    | $h_c$<br>Btu ft <sup>-2</sup> hr <sup>-1</sup> °F <sup>-1</sup> |
|---------|------------------------------------------------------------------------|-------|-----------------------------------------------------------------|
| 1       | 6.96328                                                                | 10030 | 7323.26                                                         |
| 2       | 6.99125                                                                | 10070 | 7346.78                                                         |
| 3       | 7.03774                                                                | 10137 | 7385.85                                                         |
| 4       | 6.98419                                                                | 10060 | 7340.85                                                         |
| 5       | 6.95650                                                                | 10020 | 7317.56                                                         |
| 6       | 6.98226                                                                | 10058 | 7339.56                                                         |

Table 4.3: Maximum Temperature Comparison: Full Model and Applied Heat Transfer Coefficient Function

|                                    | Full Model | Applied Function Model | % Difference |
|------------------------------------|------------|------------------------|--------------|
| Max. Temp. Target Water (°F)       | 387.185    | 346.798                | 10.43        |
| Max. Temp. Target Body (°F)        | 141.48     | 133.802                | 5.43         |
| Max. Velocity (m s <sup>-1</sup> ) | 5.4        | 5.3                    | 1.85         |

This method was applied to the newly meshed model with the original beam data, and effectively reduced the run time down to a 5 hour run time like the previous method. The maximum temperature in the target water domain was approximately 10% lower with the heat transfer coefficient interpolation function. Also, the target maximum temperatures and temperature profiles are almost identical between the two models (see Figure 4.5). The maximum velocity of the convection currents within the two models showed less than 2% difference. Since this method was within a reasonable level of accuracy and did not cause the model to exceed the saturation temperature, this method was used within the iterative process.



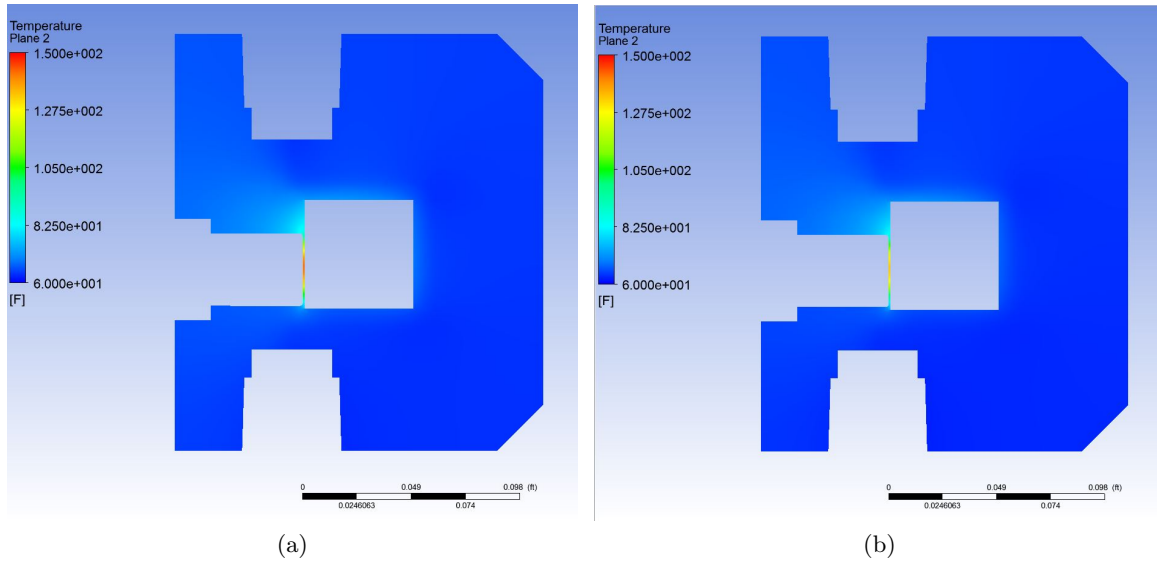


Figure 4.4: Target temperature profiles: Original (a) and HTC Function (b)

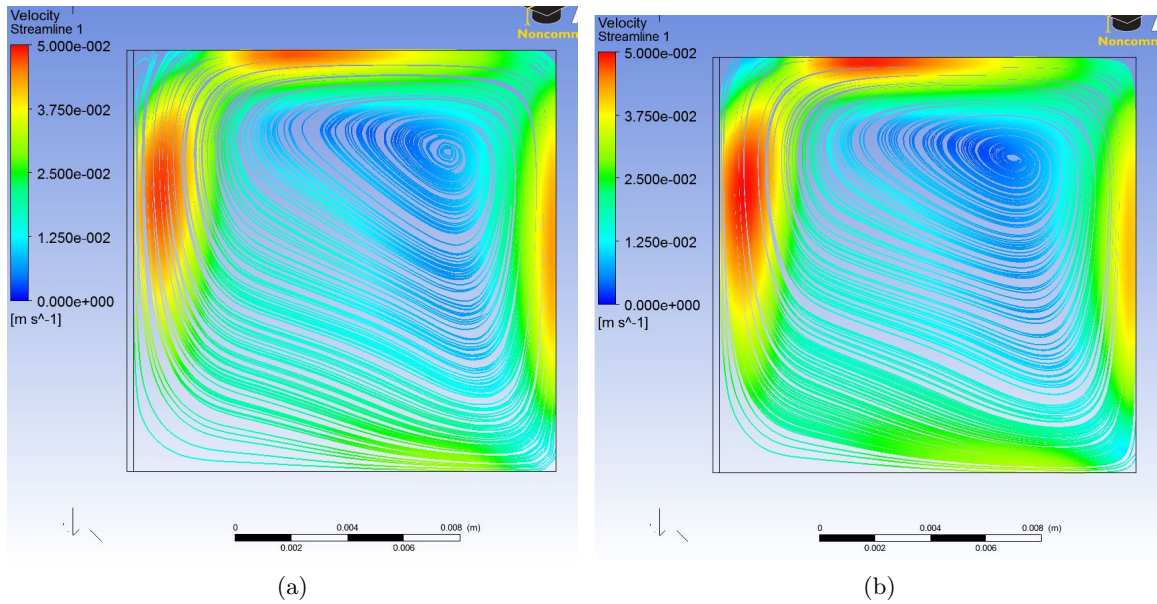


Figure 4.5: Target water velocity streamlines : Original (a) and HTC Function (b)

### MCNPX Beam Data

Another area where computational expense could be lowered was the production of the beam model. MCNPX uses a defined number of particle histories to define the beam data. An increased

number of particles provides better accuracy, but also increases the amount of time to model the beam. The particle history count was lowered to 500,000 particle histories. This beam data was used until the density residual was close to the convergence criteria. The beam was then modeled with 2,000,000 particle histories. The new beam provided better beam statistics that allowed the density and beam distribution to reach the selected convergence criteria, and required less iterations to converge since the density distribution was close to the convergence criteria from the iterations with the less expensive beam.

### **4.3.2 Mesh Study**

It was expected that the change in the beam shape would be small after the first few iterations, so a mesh that provided better resolution over the beam strike area was critical to the success of the iterative process.

#### **Decreasing Element Size**

The first change that was made to the mesh scheme was to simply reduce the size of the elements in the target water. This new mesh scheme and the resulting beam distribution is shown in Figure 4.6. While this change did effectively increase the beam resolution in the beam strike area, it also significantly increased the computational expense (from 5 hour run on 4 core machine to 36 hour run partitioned over 8 cores). This method did not meet the requirements of low computational expense and good resolution, so a new approach had to be taken.

#### **Structured Mesh**

The next mesh option explored was to apply a structured mesh across the entire target water domain. This method was unsuccessful because it was also computationally expensive because of the small cell volume required to resolve the beam area as well as provide a convergent solution. This model was run for 48 hours partitioned on 8 cores without reaching a convergent solution, so this method was abandoned.

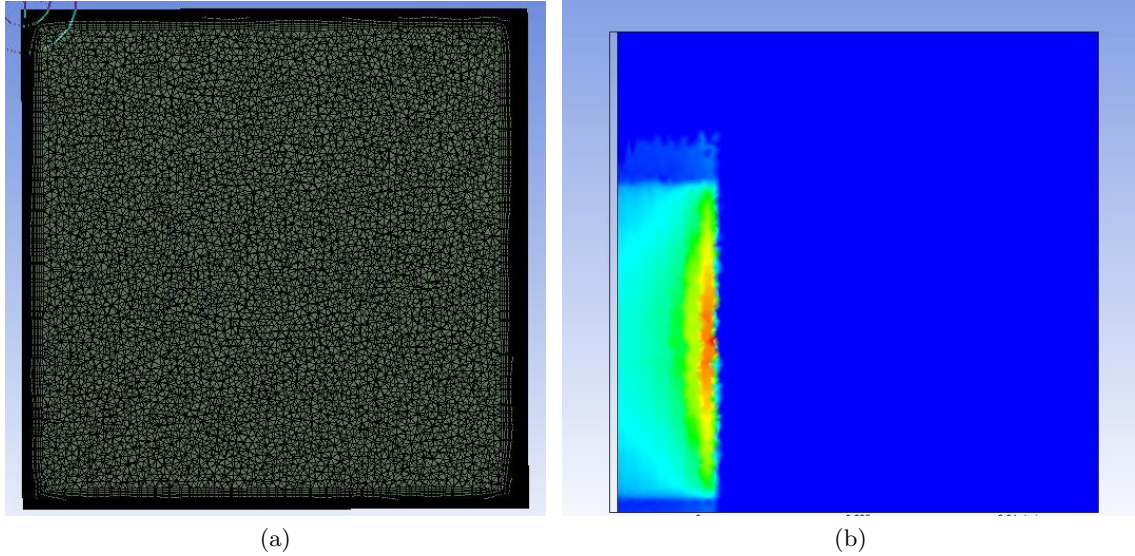


Figure 4.6: First mesh change: smaller elements

### Extended Boundary Layer

The next method to better resolve the beam strike area without significantly increasing the computational expense was extending the boundary layer of the mesh further out into the target water domain. This would allow for better resolution of the beam as it penetrates deeper into the target without the expense of meshing the entire domain with smaller elements. This method reached the convergence criteria after approximately 4 hours on the 4 core machine. Figure 4.7 shows this method does provide a resolved beam strike area at the top of the beam area. However, the lower area of the beam shows poor resolution where the boundary layers from the left and bottom surfaces meet. This method was successful in keeping computational expense low, but only partially resolved the beam, so adjustments had to be made to this method for all mesh requirements to be met.

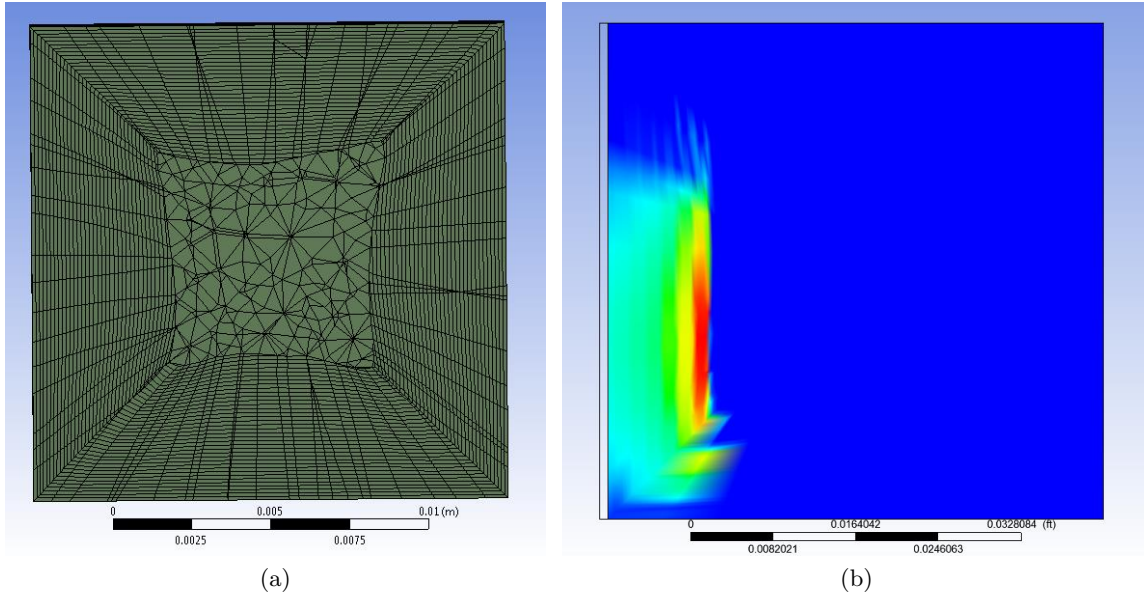


Figure 4.7: Extended Boundary Layer Mesh (a) and Beam Distribution (b)

### **Extended Boundary Layer with Bottom Layer Removed**

The previously discussed mesh was adapted by removing the bottom surface boundary layers. This new mesh scheme (reference as "adapted mesh") allows for better resolution within the beam strike area compared to the original mesh, and reached the convergence criteria within approximately 5 hours on the 4 core machine. However, this mesh removes the boundary layer from the bottom surface. The scalable wall function discussed previously still allows for an accurate solution in this area, but with poor resolution of the boundary layer velocity profile. The beam strike area is the area of the highest interest in this phase of the study, so this mesh was used for the iterative process.

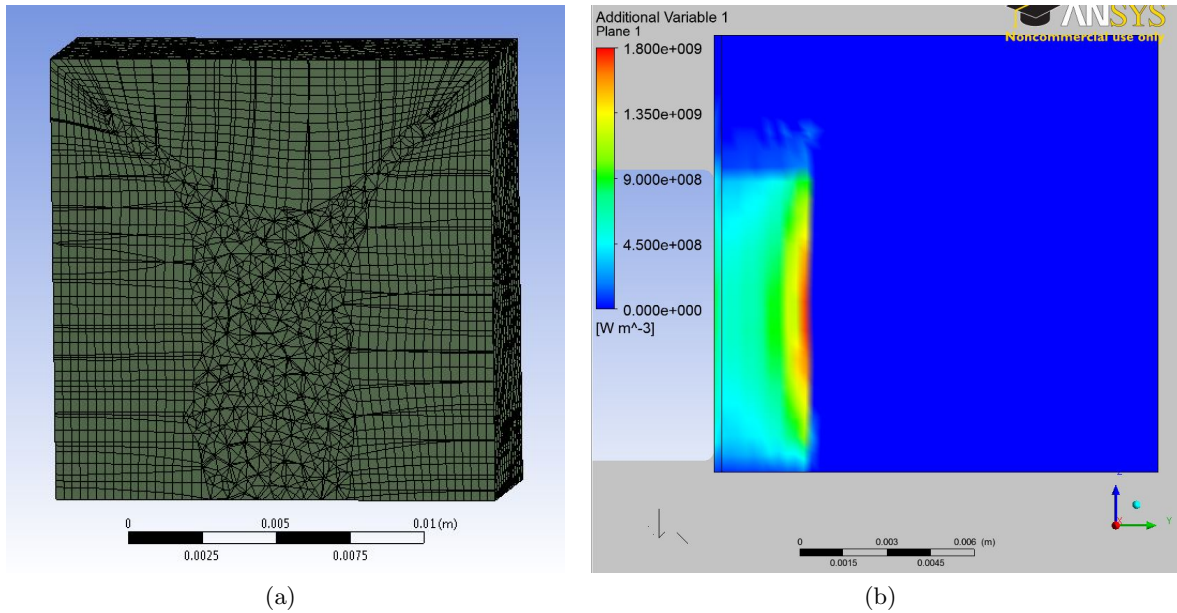


Figure 4.8: Adapted Mesh (a) and Beam Distribution (b)

## 4.4 Results

The beam and density distribution successfully reached the convergence criteria ( $1e-4$  maximum relative L-2 residual). Once the residual began to decrease very slowly but had not reached the convergence criteria, the number of particle histories in the MCNPX beam model was increased. This change in the beam definition caused a spike in the residual plot (see Figure 4.9). The beam data from the final iteration was then applied to the full target model, and the results were compared to the iterative model to confirm the iterative and full modeling methods had an acceptable level of agreement. The full model results with the new beam data were also compared to the original model results, as well as the experimental results.

In future models, the number of particle histories will be increased after the initial large drop in residual (approximately 5 iterations). This should significantly lower the number of iterations required for the density distribution to reach the specified convergence criteria.

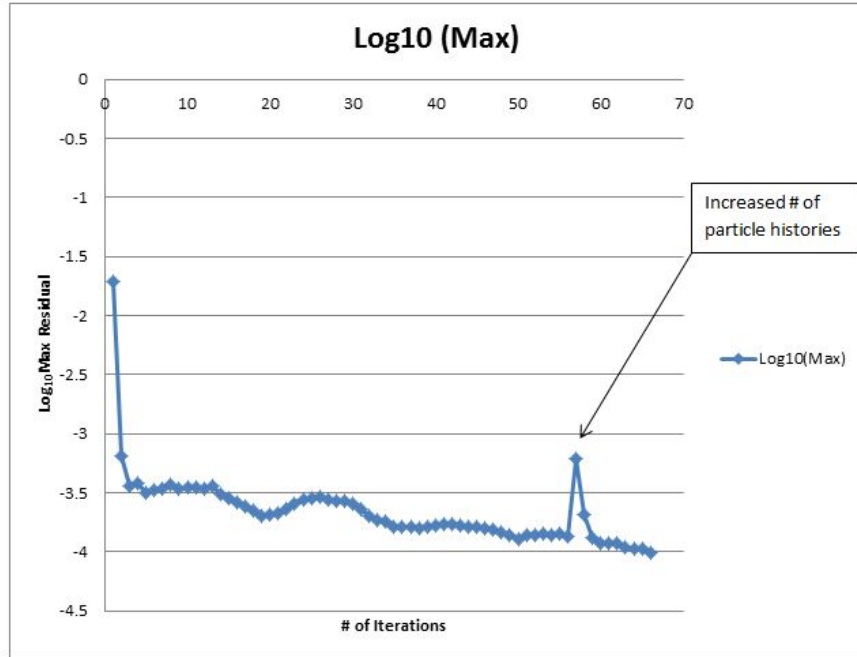


Figure 4.9: Density Residual Convergence Plot

#### 4.4.1 Full Model and Iterative Model Results Comparison

Table 4.4: Full Model and Adapted Model Comparison

|                                                   | Full Model | Adapted Model | % Difference |
|---------------------------------------------------|------------|---------------|--------------|
| Max. Temp: Target Body ( $^{\circ}\text{F}$ )     | 143.3534   | 142.1402      | 0.846        |
| Max. Temp: Sapphire ( $^{\circ}\text{F}$ )        | 338.2196   | 332.0240      | 1.832        |
| Max. Temp: Target Water ( $^{\circ}\text{F}$ )    | 389.8688   | 383.3384      | 1.675        |
| Max. Velocity: Target Water ( $\text{m s}^{-1}$ ) | 0.058563   | 0.0575216     | 1.778        |

The maximum domain temperatures and target water fluid velocities for the full and iterative models with the same beam data are given in Table 4.4. The beam data distributions



are shown for each model in Figure 4.10. The beam data from the two models are identical, so the maximum volumetric heat generation rate is the same for both models. The temperature distributions in the target and target water (Figures 4.11 and 4.12) show excellent agreement, with maximum temperatures in the same location and less than 2% difference. A temperature difference profile for the target water between the Full model and the Iterative model is shown in Figure 4.13. The velocity differences between the two models also show less than 2% difference. There is excellent agreement between the full model and the adapted model, so the methods used to decrease the computational expense were successful and gave results with an acceptable level of agreement between the two models.

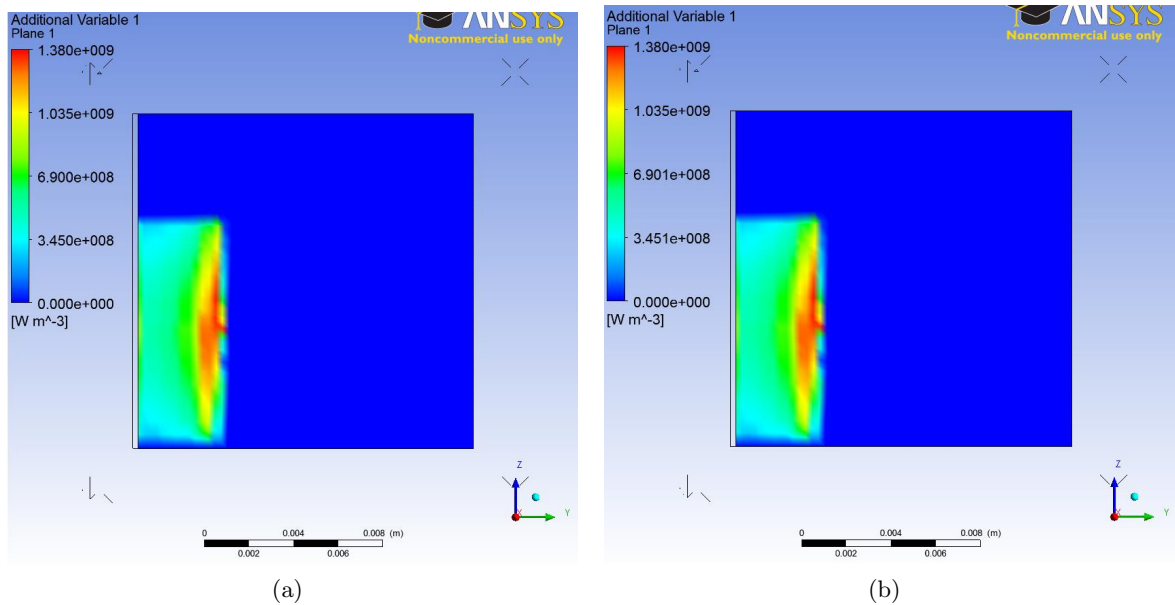


Figure 4.10: Full (a) and Iterative (b) Model Beam Distributions

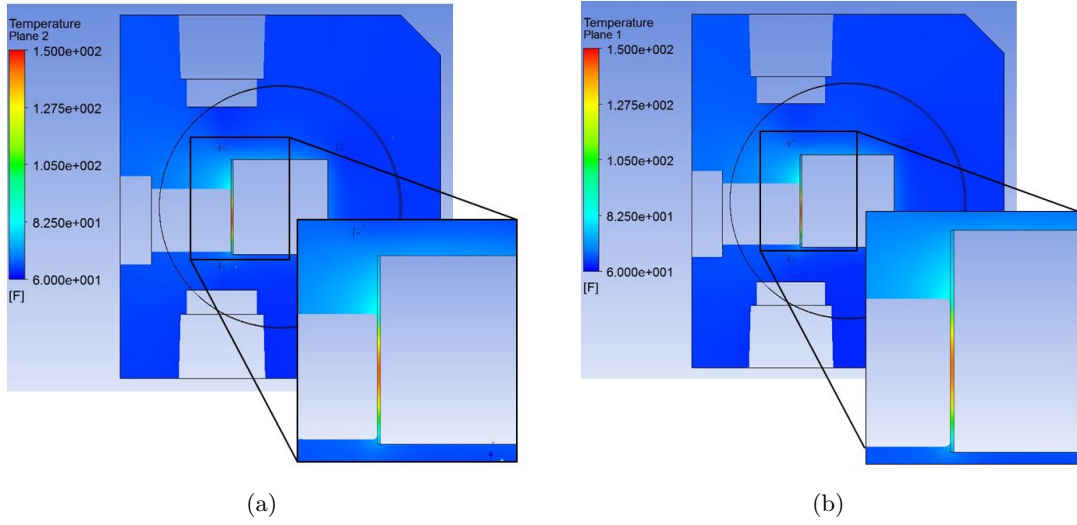


Figure 4.11: Full (a) and Iterative (b) Models Target Body Temperature Distributions

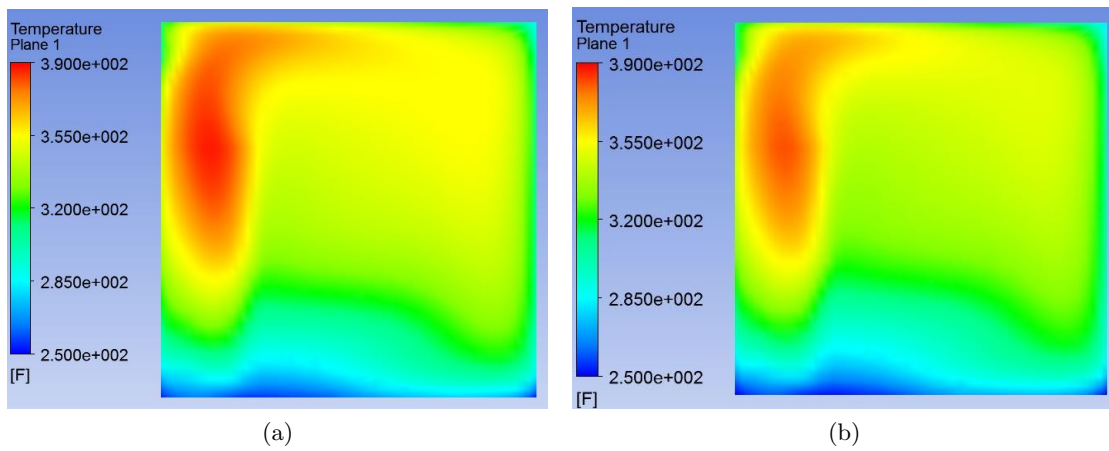


Figure 4.12: Full (a) and Iterative (b) Models Target Water Temperature Distributions



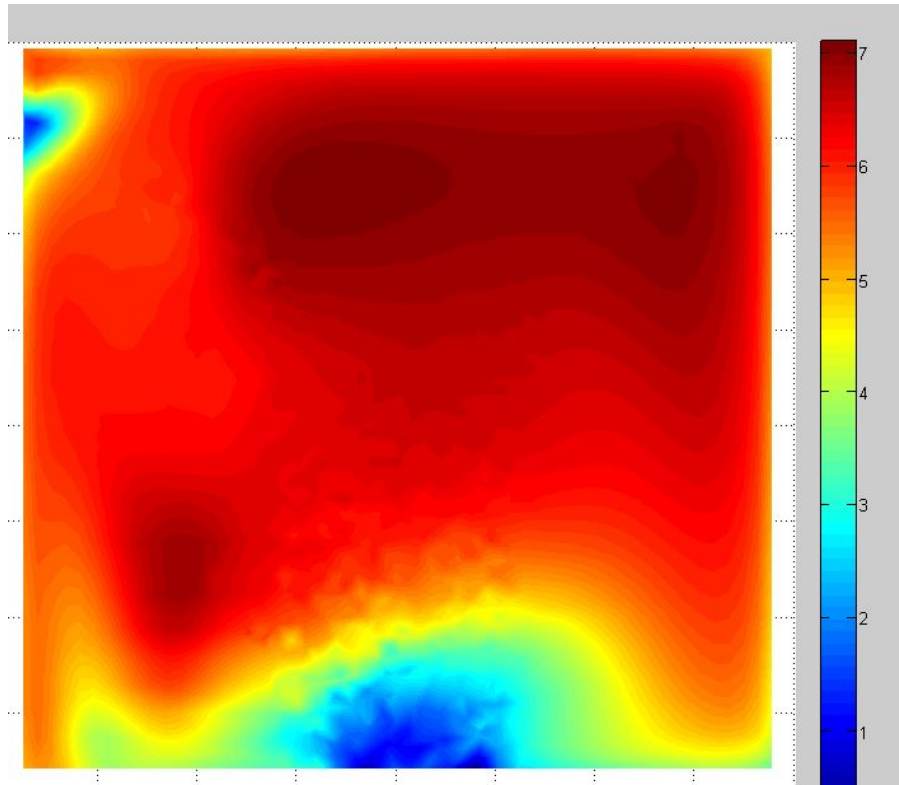


Figure 4.13: Target Water Temperature Difference ( $\Delta T$ ) in  $^{\circ}\text{F}$

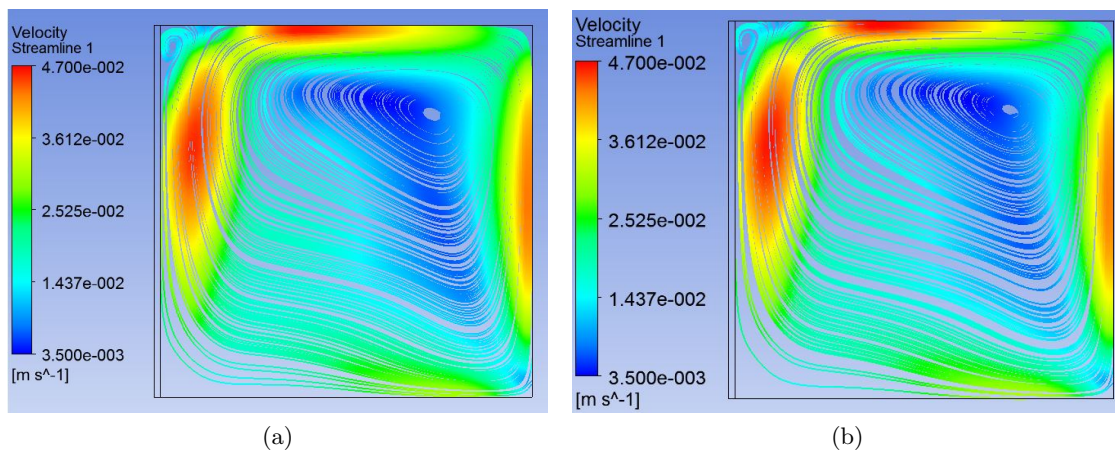


Figure 4.14: Full (a) and Iterative (b) Models Target Water Velocity Streamlines

#### 4.4.2 Original and Iterated Beam Comparison

To study the effect of coupling the beam data with the density distribution of the target water, the iterated beam data was compared to the original beam data (uniform density distribution).

Table 4.5: Original Beam vs. Iterated Beam

|                                   | Original              | Iterated              |
|-----------------------------------|-----------------------|-----------------------|
| Beam Range (mm)                   | 3.10                  | 4.05                  |
| Max. $Q'''$ ( $W\ m^{-3}$ )       | $1.72793 \times 10^9$ | $1.38028 \times 10^9$ |
| Max. Temperature ( $^{\circ} F$ ) | 362.77                | 383.34                |

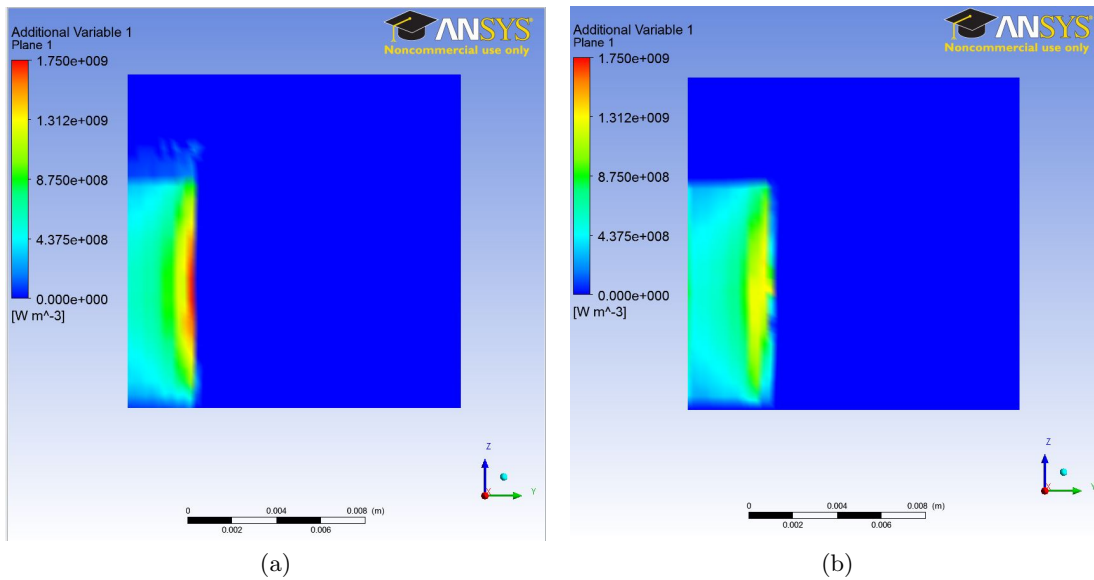


Figure 4.15: Original (a) and Iterated (b) Beam Distributions

As expected, the density dependent (iterated) beam penetrates further into the target water

than the density independent beam. The maximum volumetric heat generation rate is greater in the original beam. The density dependent beam has a broader Bragg Peak region, giving less intense area of maximum heat generation. A line plot of the volumetric heat generation rate through the center of the beam is shown in Figure 4.16. Though the maximum value of the energy deposition was lower, the iterated beam model had a higher maximum temperature.

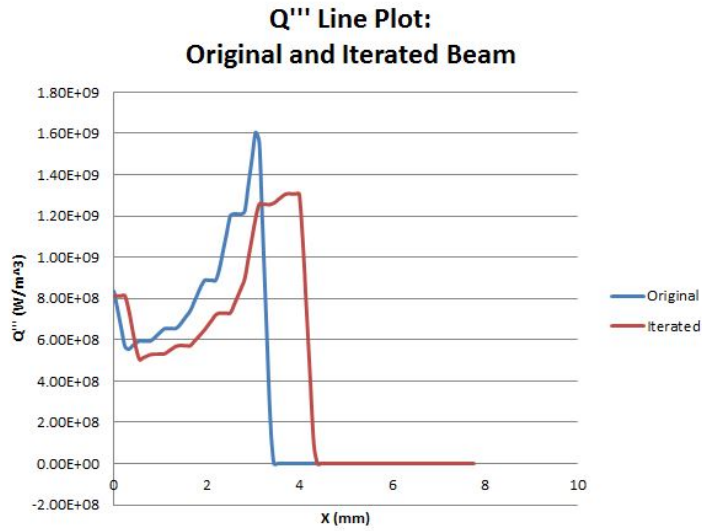


Figure 4.16: Line Plot - Original and Iterated Beam Centerline

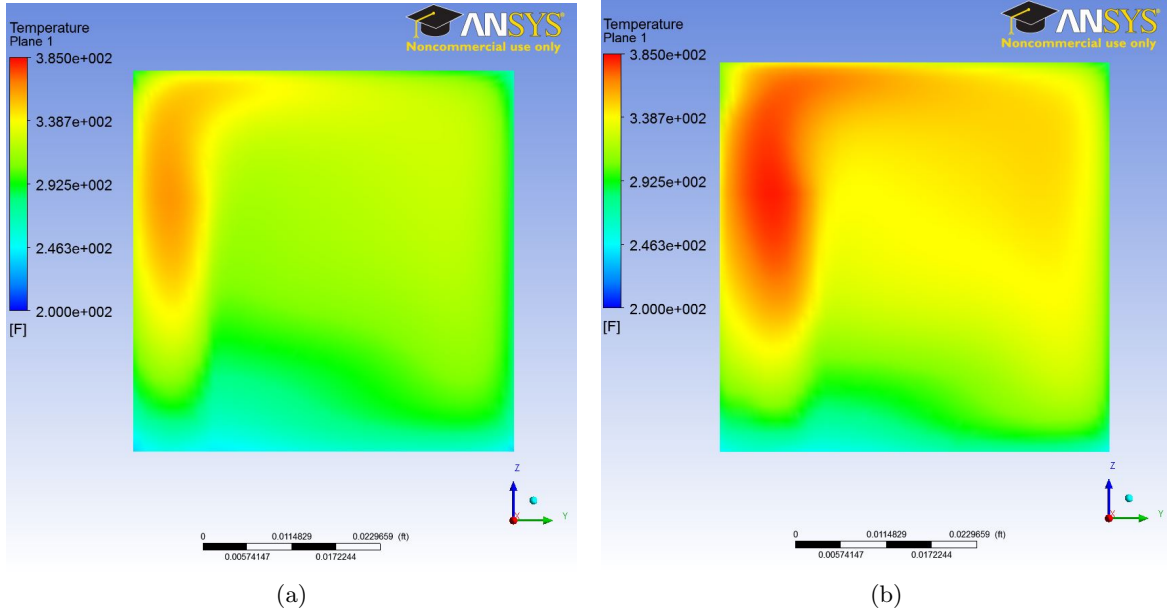


Figure 4.17: Original (a) and Iterated (b) Temperature Distributions

#### 4.4.3 Experimental Validation

Analysis of the experimental video gives an approximate fluid velocity of 5-10 cm/s for a partial fill operated at 300 psi with a 9  $\mu$ A beam of 18 MeV protons. While the computational model is not an exact replication of the experimental parameters, it is reasonable to have confidence in the computational model as the velocity is within the same order of magnitude. Also, the proton beam range in the experimental video is approximately 4 mm. This also agrees with the results of the iterated beam model, giving confidence that this modeling approach is more accurate than the uniform beam model, and can be used to model other target geometries and operating conditions.

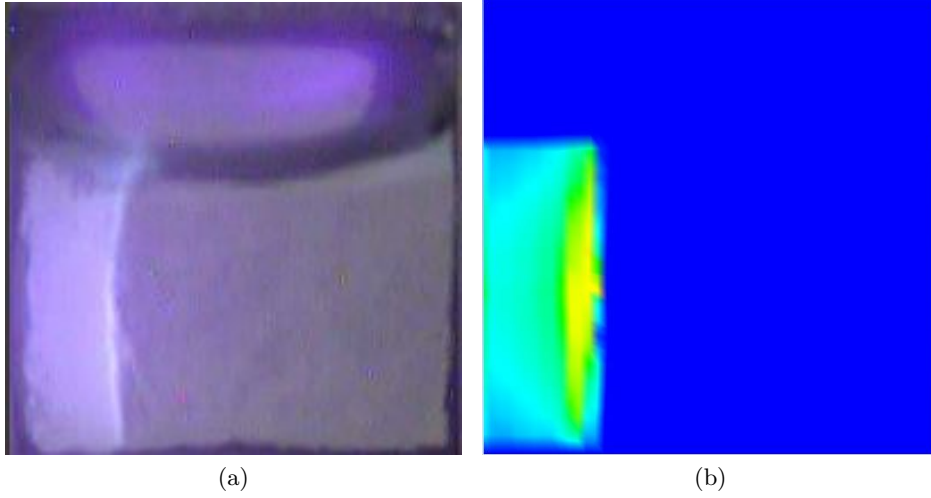


Figure 4.18: Experimental and Computational Beams

# Chapter 5

## Conclusion

The computational model successfully coupled the MCNPX beam data with the fluid property distribution from ANSYS CFX. Applying the density distribution to the MCNPX model definition increased the proton beam range by 0.95 mm (30.65%), and also resulted in a broad, less intense Bragg peak. The proton beam range and velocity profiles between experimental and computational results offer good agreement, giving confidence that this technique can be used to model the thermal performance of other target geometries.

### 5.1 Future Work

The next phase of this model is to apply the Homogenous Equilibrium Model (HEM) as a method of modeling the transition from single phase liquid to boiling. The HEM method assumes that the fluid and vapor phases have equal velocities and are in thermodynamic equilibrium. This can be achieved by modifying the state equations within ANSYS CFX.

Using the results from this computational model, two other target designs have been developed to potentially increase the thermal capacity of the target system. The computational model explored in this project will also be applied to those geometries. Preliminary work on these two designs is shown in Appendix C and Appendix D.

Other work will include using this coupling technique on a gas target model. The energy

deposition and beam shape is expected to be coupled much tighter to the density distribution for these targets because vapor density fluctuates much more with changes in temperature than liquid.

Another possible direction is to apply the iterative process to a multi-phase capable CFD software. When a liquid transitions to the vapor phase, there is a significant change in density, producing a large increase in the proton beam range. A computational model that is capable of coupling the proton beam data to the fluid density and void distributions will be a powerful tool in finding optimum operating conditions for boiling water targets.

## REFERENCES

- [1] *ANSYS CFX 14.0 Manual*.
- [2] *MCNPX<sup>TM</sup> USER'S MANUAL*.
- [3] Iba cyclone, 2013.
- [4] FEATFLOW. High performance finite elements: Used cfd software packages.
- [5] MolTech Gmbh. Sapphire al2o3, 2013.
- [6] Sven-Johan Heselius, Peter Lindblom, and Olof Solin. Optical studies of the influence of an intense ion beam on high-pressure gas targets. *The International Journal of Applied Radiation and Isotopes*, 33(8):653 – 659, 1982.
- [7] Bong Hwan Hong, Tea Gun Yang, In Su Jung, Yeun Soo Park, and Hyung Hee Cho. Visualization experiment of 30 mev proton beam irradiated water target. *Nuclear Instruments and Methods in Physics Research Section A: Accelerators, Spectrometers, Detectors and Associated Equipment*, 655(1):103 – 107, 2011. Proceedings of the 25th World Conference of the International Nuclear Target Development Society.
- [8] B.E. Launder and D.B. Spalding. The numerical computation of turbulent flows. *Computer Methods in Applied Mechanics and Engineering*, 3(2):269 – 289, 1974.
- [9] M. Nallasamy. Turbulence models and their applications to the prediction of internal flows: A review. *Computers and Fluids*, 15(2):151 – 194, 1987.
- [10] J. L. Peeples, M. H. Stokely, M. C. Poorman, M. Magerl, and B. W. Wieland. Visual observation of boiling in high power liquid target. In M. A. Avila-Rodriguez, J. P. O'Neil, T. E. Barnhart, D. W. Dick, J. Kozirowski, S. Lapi, and J. S. Lewis, editors, *American Institute of Physics Conference Series*, volume 1509 of *American Institute of Physics Conference Series*, pages 76–80, December 2012.



- [11] Johanna L. Peeples, Matthew H. Stokely, and J. Michael Doster. Thermal performance of batch boiling water targets for  $^{18}\text{F}$  production. *Applied Radiation and Isotopes*, 69(10):1349 – 1354, 2011.
- [12] M.E. Phelps. *PET Molecular Imaging and its Biological Applications*. Springer-Verlag, 2004.
- [13] S. Sahling, J. Engert, A. Gladun, and R. Knoner. The thermal boundary resistance between sapphire and aluminum monocrystals at low temperature. *Journal of Low Temperature Physics*, 45(5-6):457–469, 1981.
- [14] James E. Turner. *Atoms, Radiation, and Radiation Protection*. WILEY-VCH, 2007.

## APPENDICES

# Appendix A

## MCNPX Input File Example

```
18 MeV Protons in Water
c Mesh Energy Deposition
c
c
c --- cell cards ---
c
c
c Aluminum
  1 1 -2.810 -1 2 -3 imp:h=1
c WATER
  2 2 -1 -1 3 -4 imp:h=1
c OUTSIDE UNIVERSE
  3 0 1:-2:4 imp:h=0

c --- surface cards ---
c
  1 cz 0.5
  2 pz 0.0
  3 pz 0.0127
  4 pz 1.0

c --- material cards ---
c
c Material #1: Aluminum
m1 13027 -1
c Material #2: H2O
m2 HLIB=24h 1001.24h -0.1119 8016.24h -0.8881
c --- data cards ---
mode h
phys:h 18.0 j 0. j
cut:h 0.05
c mode is set to protons with the energy range 18 MeV max and 50
```

```
      keV min
lca j j j
nps 100000
F1:H 2
c the next 7 lines are the energy deposition mesh
TMESH
CMESH3 total
ERESH3 0.0 18.0
  CORA3 0.0 0.013157895655 17i 0.486842104345 0.5
  CORB3 0.0 0.023684211204 17i 0.876315788796 0.9
  CORC3 360
ENDMD
c
c --- source definition ---
c 18 MeV Proton Beam
SDEF SUR=2 DIR=1 vec=0. 0. 1. erg=18. PAR=h pos=0. 0. 0. x=d5 y=
  d3 z=0 CCC=1
SC3 Gaussian Distribution with 50% at 5.0 mm
SP3 -41 0.99868 0
SC5 Gaussian Distribution with 50% at 5.0 mm
SP5 -41 0.99868 0
```

# Appendix B

**ANSYS CFX Solver: Residual Convergence Plots**

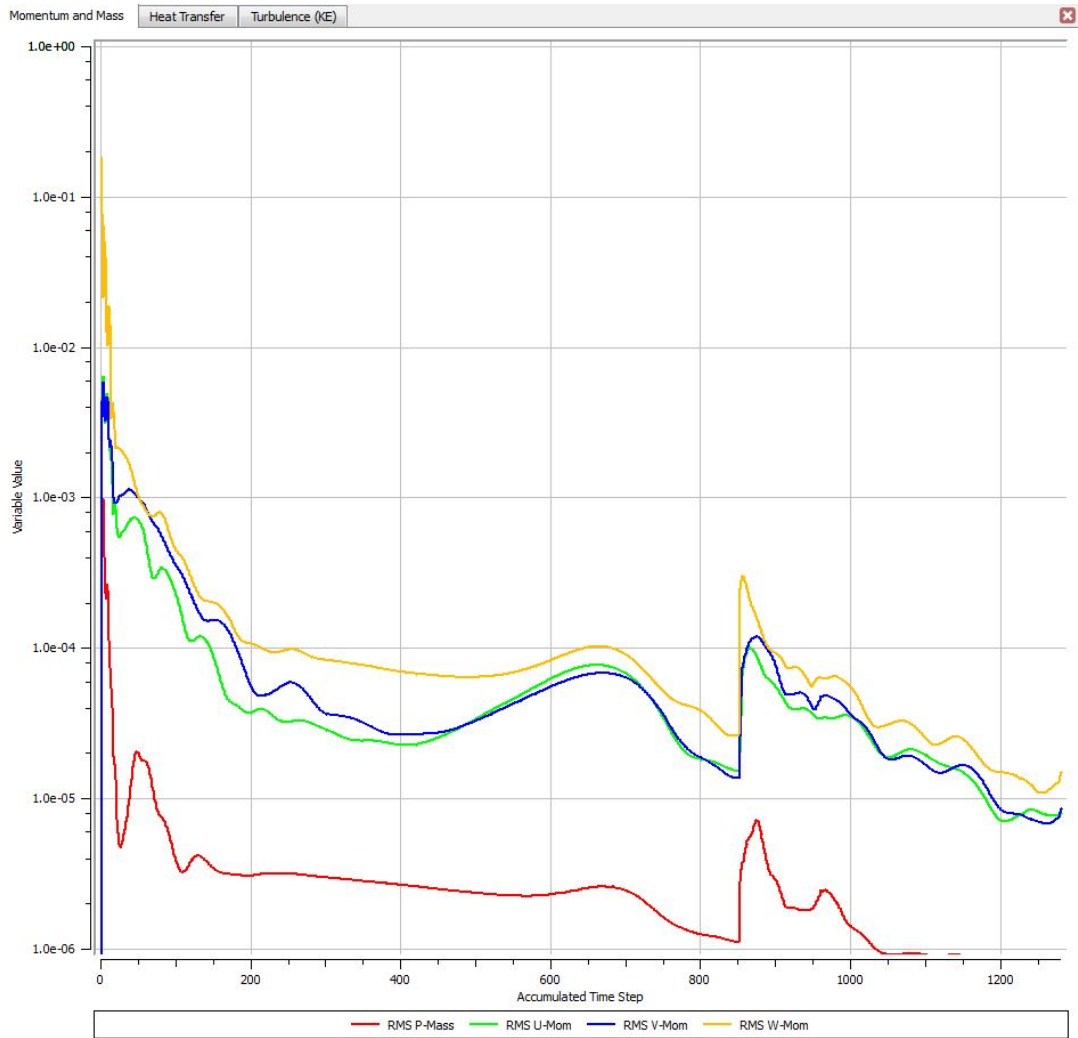


Figure B.1: Momentum and Mass Residual Plot

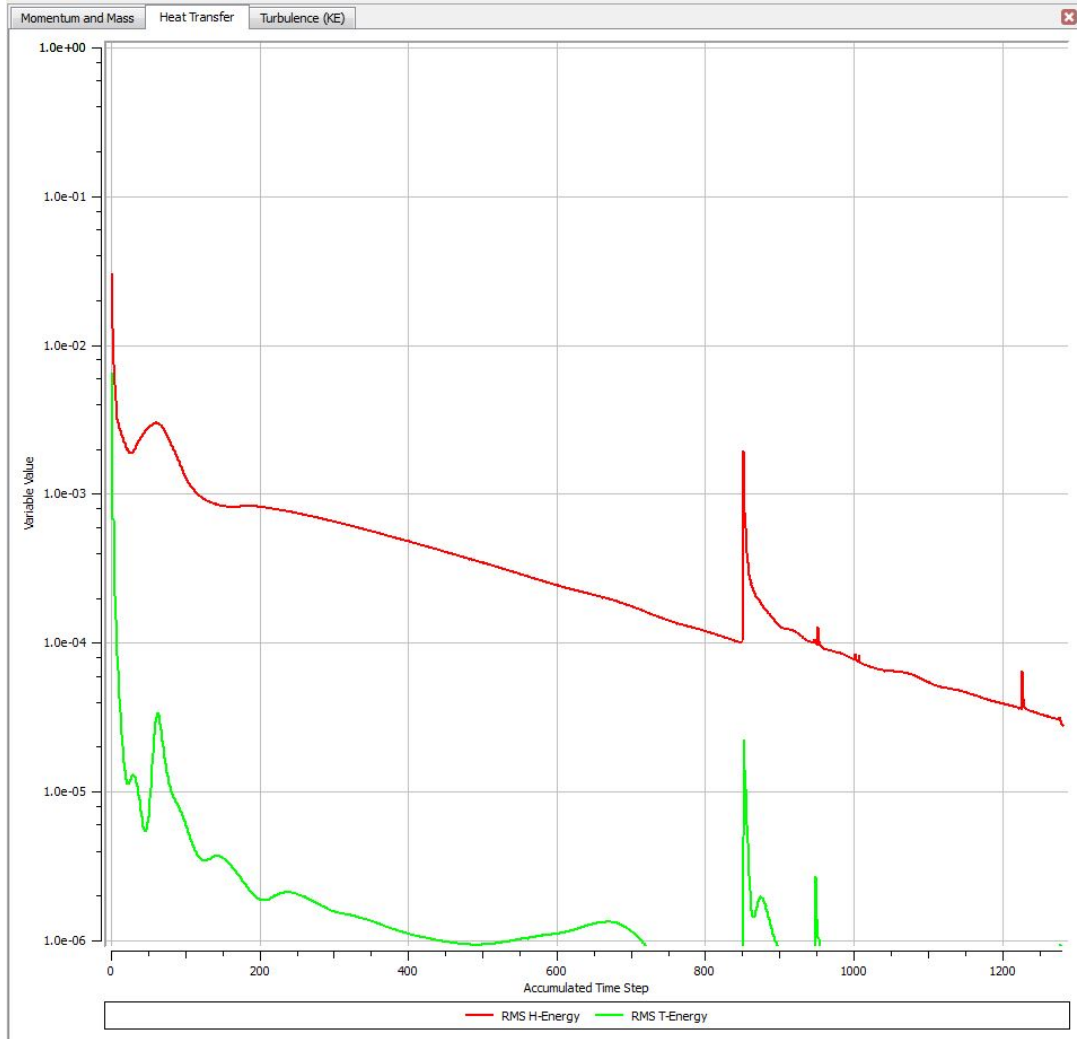


Figure B.2: Heat Transfer Residual Plot

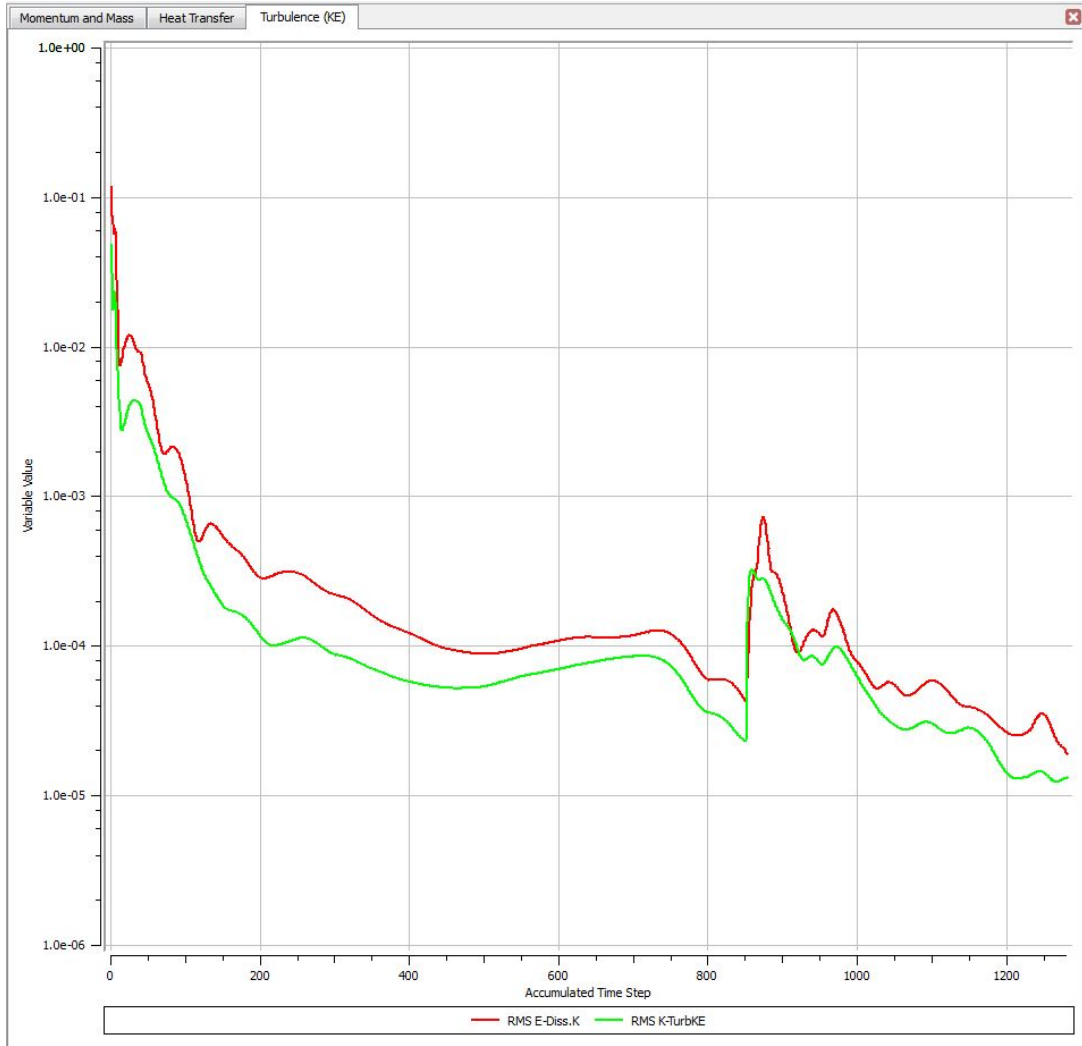


Figure B.3: Turbulence (KE) Residual Plot



# Appendix C

## Rectangle Visualization Geometry

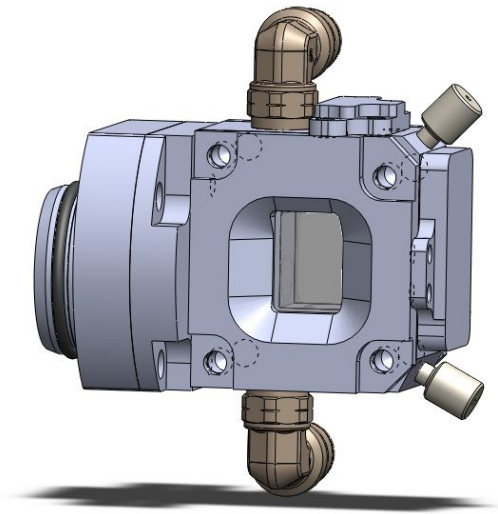


Figure C.1: CAD Model: Rectangular Target

A new visualization target was designed to have a taller target water chamber. The taller target has a larger condensing region at the top of the target water chamber, allowing for better cooling when the target water transitions to two-phase boiling. This also allows for a

larger beam diameter (12 mm), which should result in a lower maximum temperature at the Bragg peak for the same particle energy and beam currents. Preliminary modeling has been performed on this geometry (initial mesh setup, uniform density beam data, and full coolant solution).

Table C.1: Rectangle Model: Maximum Temperatures

| Domain       | Maximum Temperature °F |
|--------------|------------------------|
| Target       | 138.48                 |
| Sapphire     | 263.20                 |
| Target Water | 305.82                 |
| Coolant      | 62.15                  |

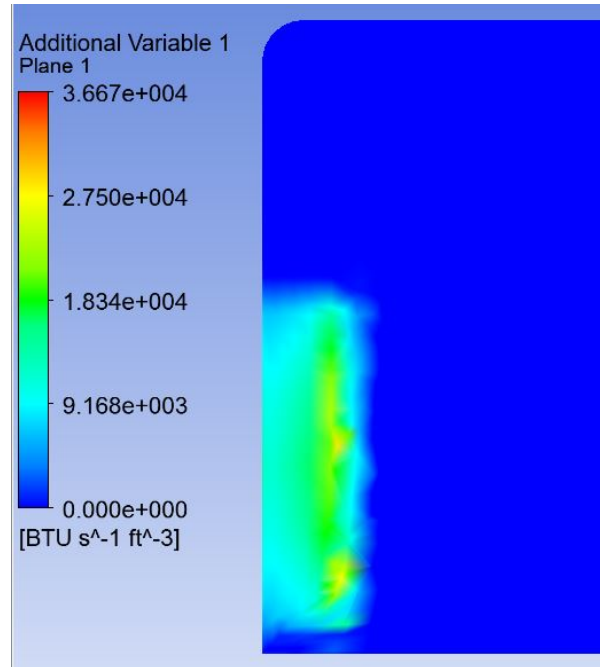


Figure C.2: Rectangle Model: Energy Deposition Distribution

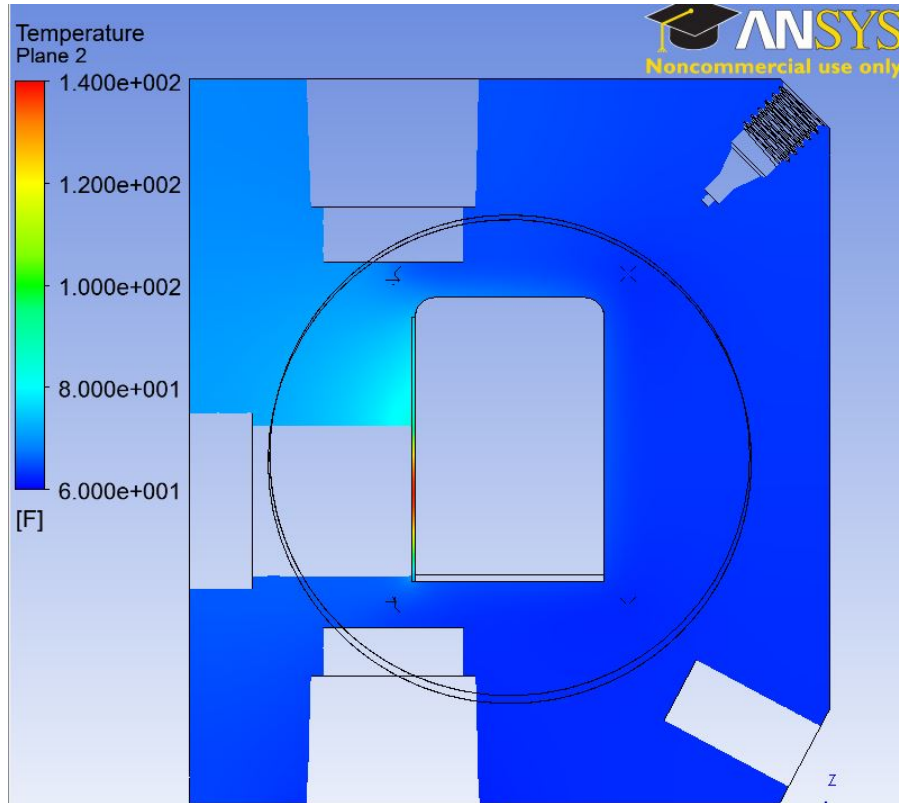


Figure C.3: Rectangle Model: Target Temperature Distribution

From the initial model results, the new target geometry has successfully increased the thermal capacity of the target system. The maximum temperatures in the target and target water are lower in the Rectangle visualization target than the original visualization target, and are located in the same corresponding areas as in the original model (Figures C.3 and D.3). The convection currents within the target water are also very clearly shown in Figure D.4.

This model will be adapted with the applied heat transfer coefficient interpolation function as well as meshed with the extended boundary layer to properly resolve the beam strike area. A study was completed on this model to find the beam current that results in a maximum target water temperature exceeding the saturation temperature. These results are given in Table C.2.

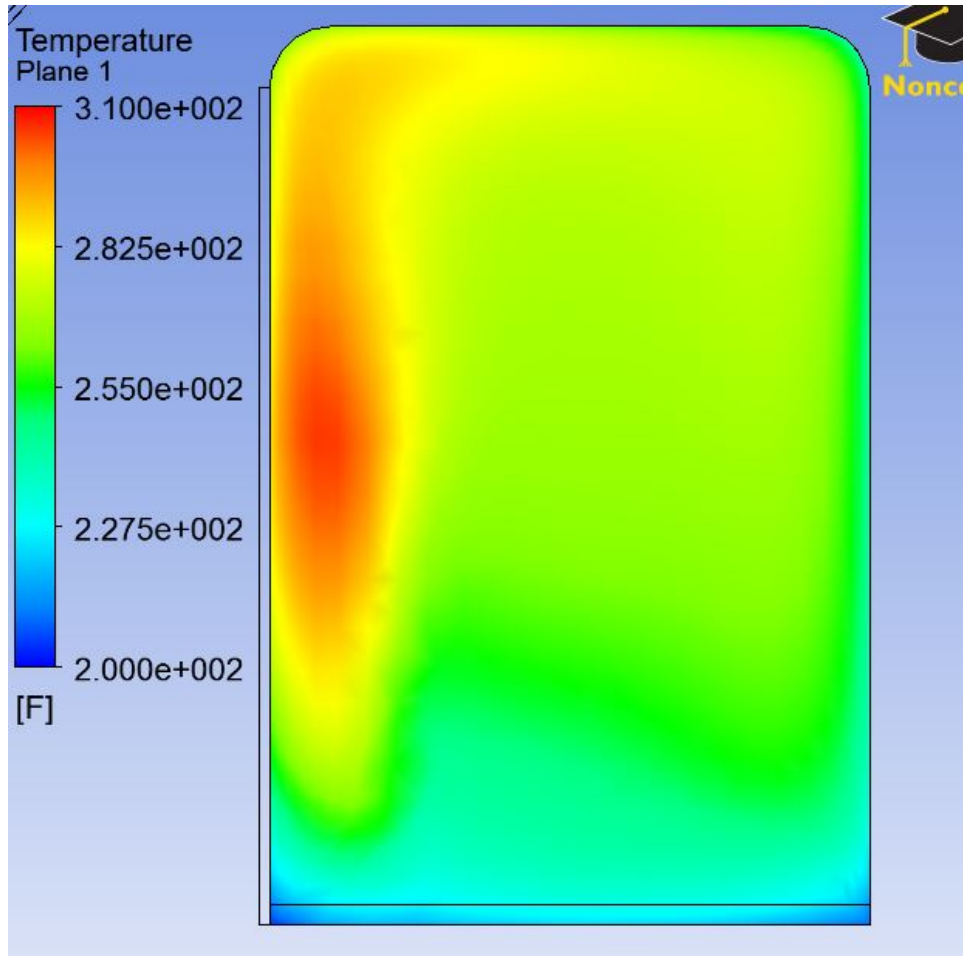


Figure C.4: Rectangle Model: Target Water Temperature Distribution

Table C.2: Rectangle Model: Saturation Temperature Study Results

| Beam Current ( $\mu\text{A}$ ) | Maximum Temperature ( $^{\circ}\text{F}$ ) |
|--------------------------------|--------------------------------------------|
| 10                             | 305.823                                    |
| 15                             | 360.967                                    |
| 20                             | 407.268                                    |
| 25                             | 447.444                                    |
| Saturation Temperature         | 444.616                                    |

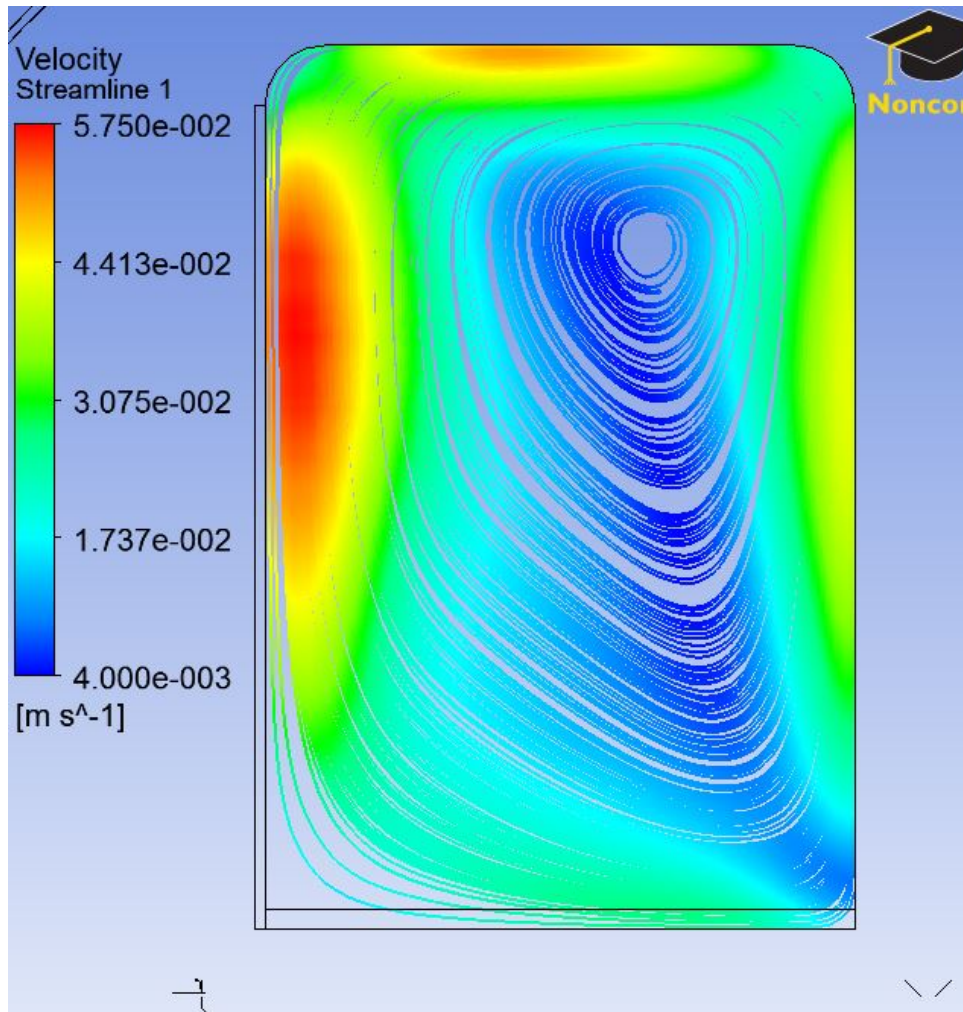


Figure C.5: Rectangle Model: Target Water Velocity Streamlines

# Appendix D

## Slanted Visualization Geometry

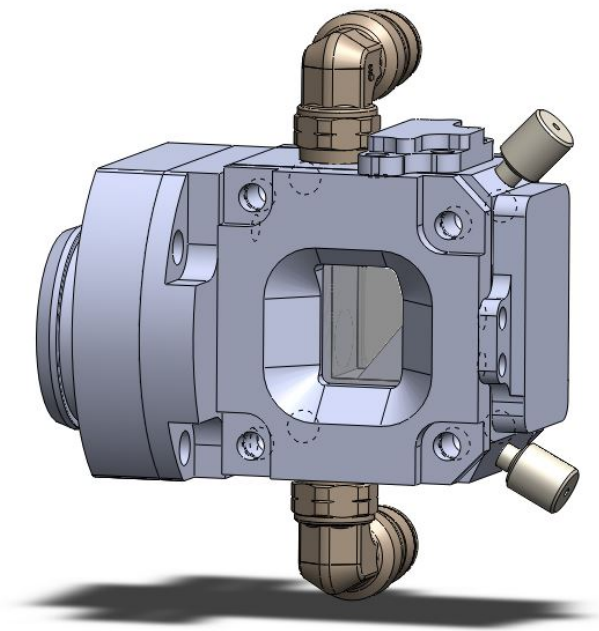


Figure D.1: CAD Model: Slant Target

A Slanted target geometry was designed to reduce the total volume of the Rectangle target

geometry. A slanted back wall was added to remove a portion of the target water chamber without affecting the natural circulation currents within the target chamber. This model has proven to be computationally very expensive. The amount of time necessary to reach the default convergence criteria exceeds 240 hours when partitioned 8 times on 8 cores. Decreasing the computational expense of this model will be a priority before future work can be completed.

The results shown below do not provide an accurate comparison to the results for the Rectangle model given in Appendix C because this model was run without a contact resistance specified between the sapphire windows and target body. This model was run prior to the value of contact resistance being provided. Though it is not appropriate to compare these results to the results in Appendix C, the results will provide insight into the temperature distribution and velocity profile.

The location of the maximum temperatures correspond to the same locations as the Rectangle model. The overall shape of the natural circulation currents have changed due to the slanted back wall of the target water chamber, but are still very apparent and have not been disrupted by the change in the target design.

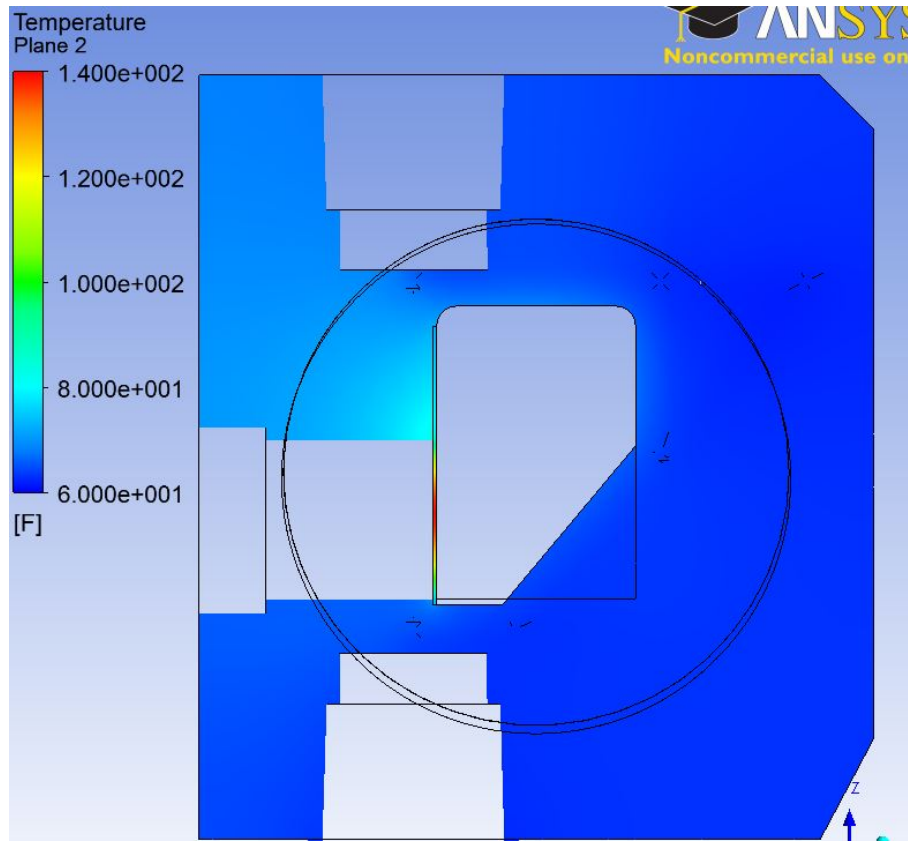


Figure D.2: Slanted Model: Target Temperature Distribution



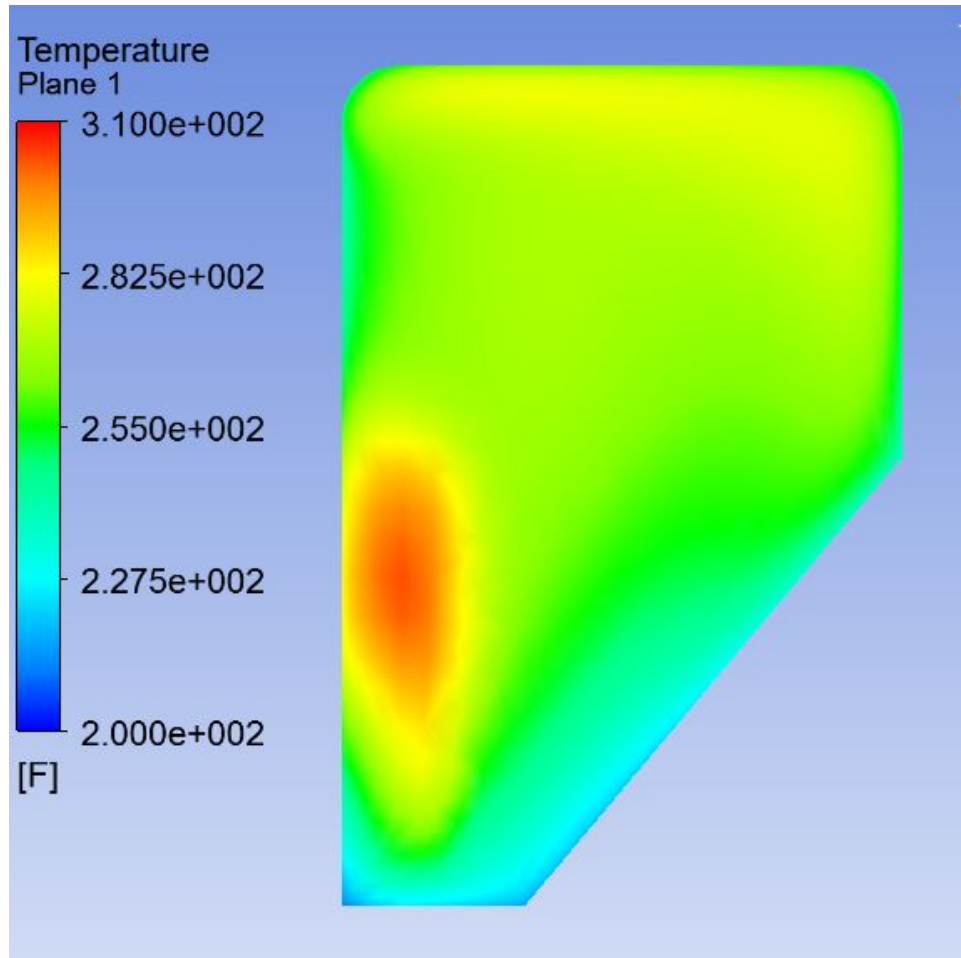


Figure D.3: Slanted Model: Target Water Temperature Distribution

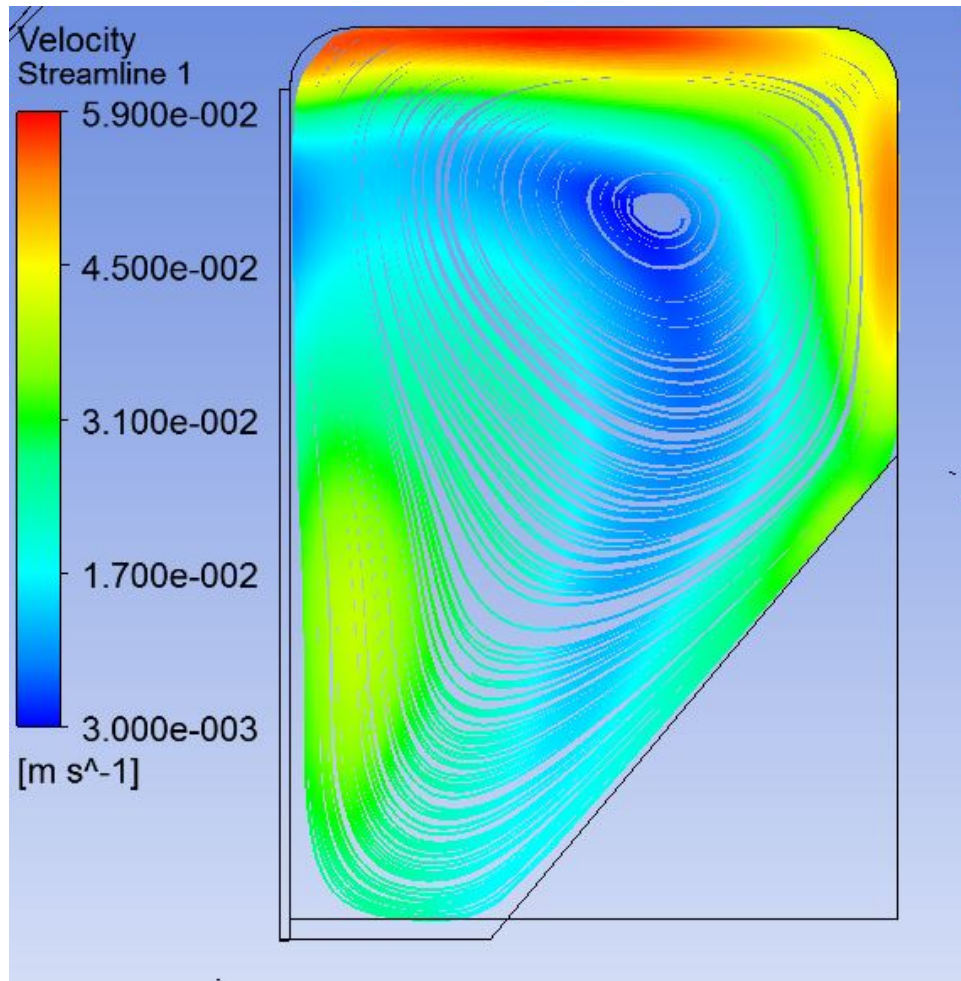


Figure D.4: Rectangle Model: Target Water Velocity Streamlines